

JGR Solid Earth

RESEARCH ARTICLE

10.1029/2020JB020588

Key Points:

- Highly magnetic red soil on low-magnetic bedrock is dominated by ~10- to 15-nm-sized magnetite forming ~100-nm aggregates with SP-SSD behavior
- During transfer of red soil material to lake sediments, the aggregates partly disintegrate resulting in domain states with lower χ and $\chi_{fd}\%$
- SIRM/ χ in red soil represents the specific arrangement of nano-magnetite particles in the aggregates and is a potential paleoclimate proxy

Supporting Information:

- Supporting Information S1

Correspondence to:

E. Appel,
erwin.appel@uni-tuebingen.de

Citation:

Zhang, Q., Appel, E., Hu, S., Pennington, R. S., Meyer, J., Neumann, U., et al. (2020). Nano-magnetite aggregates in red soil on low magnetic bedrock, their changes during source-sink transfer, and implications for paleoclimate studies. *Journal of Geophysical Research: Solid Earth*, 125, e2020JB020588. <https://doi.org/10.1029/2020JB020588>

Received 20 JUL 2020





Accepted 12 SEP 2020

Accepted article online 17 SEP 2020

©2020. The Authors.

This is an open access article under the terms of the Creative Commons Attribution License, which permits use, distribution and reproduction in any medium, provided the original work is properly cited.

Nano-Magnetite Aggregates in Red Soil on Low Magnetic Bedrock, Their Changes During Source-Sink Transfer, and Implications for Paleoclimate Studies

Qi Zhang¹ , Erwin Appel¹ , Shouyun Hu², Robert S. Pennington^{3,4,5}, Jannik Meyer^{3,4}, Udo Neumann¹, Michael Burchard⁶, Frederik Allstädt⁶ , Longsheng Wang⁷, and Andreas Koutsodendris⁶ 

¹Department of Geosciences, University of Tübingen, Tübingen, Germany, ²Nanjing Institute of Geography and Limnology, Chinese Academy of Sciences, Nanjing, China, ³Institute of Applied Physics, University of Tübingen, Tübingen, Germany, ⁴NMI Natural and Medical Sciences Institute, University of Tübingen, Reutlingen, Germany, ⁵Department of Physics, Humboldt-Universität zu Berlin, Berlin, Germany, ⁶Institute of Earth Sciences, Heidelberg University, Heidelberg, Germany, ⁷Coast Institute, Ludong University, Yantai, China

Abstract Soil and lake sediments are important paleoclimate archives often forming a source-sink setting. To better understand magnetic properties in such settings, we studied red soil on low-magnetic bedrock and subrecent sediments of Caohai Lake (CL) in Heqing Basin, China. Red soil is the only important source material for the CL sediments, it is highly magnetic with susceptibilities (χ) of $\sim 10^{-5}$ m³/kg. The red soil is dominated by pedogenic nano-magnetite (~10–15 nm) arranged in aggregates of ~100 nm, with particle interaction that causes a wide effective grain size distribution in the superparamagnetic (SP) range tailing into stable single-domain behavior. Transmission electron microscopy and broadband frequency $\chi(f)$ suggest partial disintegration of the aggregates and increased alteration of the nanoparticles to hematite during transfer of red soil material to CL. This shifts the domain state behavior to smaller effective magnetic grain sizes, resulting in lower $\chi_{fd}\%$ and χ values, and a characteristic change of $\chi(f)$. The SP-stable single-domain distribution of the aggregates in red soil could be climate dependent, and the ratio of saturation remanence to χ is a potential bedrock-specific paleoclimate proxy reflecting it. Magnetic properties of the CL sediments are controlled by an assemblage of nanoparticle aggregates and larger-sized bedrock-derived magnetite. The results challenge the validity of the previous paleoclimate interpretation from the 168-m-long Core-HQ (900–30 ka) in Heqing Basin. Disintegration of aggregates could lead to SP behavior with low $\chi_{fd}\%$ without extinction of individual magnetite nanoparticles, and the $\chi_{fd}\%$ -based assumption of SP magnetite dissolution may be wrong.

1. Introduction

Soil properties can serve as an important indicator for paleoclimate conditions (Tabor & Myers, 2015). Soil also contributes as source material for basin deposits such as lake sediments (Lavrieux et al., 2019). In settings where the catchment is well defined and where soil is the major source for lake sediments, the relationship between the source (soil) and the sink (lake sediment) can be systematically studied.

Lake sediments are important paleoclimate archives (An et al., 2011; Gasse et al., 1991; Koutsodendris et al., 2018). Magnetic properties were often used to deduce information on paleoenvironmental conditions and processes (Geiss et al., 2003; Hu et al., 2015; Peck et al., 1994). The origin of ferro(i)magnetic minerals in lake sediments is either detrital or authigenic. Magnetic minerals from the catchment transported to lakes by surface water or wind may reach their sink without notable changes, but often they are subjected to alteration such as change or fractionation of grain size and mineral transformation (Oldfield & Robinson, 1985; Snowball, 1993). Ferro(i)magnetic minerals can form authigenically in lake sediments by inorganic processes (Maher & Taylor, 1988) or through bacterial activity (Kodama, 2013). Biomineralization also happens in soil, forming magnetosomes (Fassbinder et al., 1990) and extracellular magnetite (Maher, 1998). The complexity of magnetic mineral sources and the possible change of their properties during transport and residence time in lake sediments are a great challenge when using magnetic properties as paleoenvironmental proxy. Environmental magnetic studies of lake sediments mostly focus on proxies recorded in drill cores,

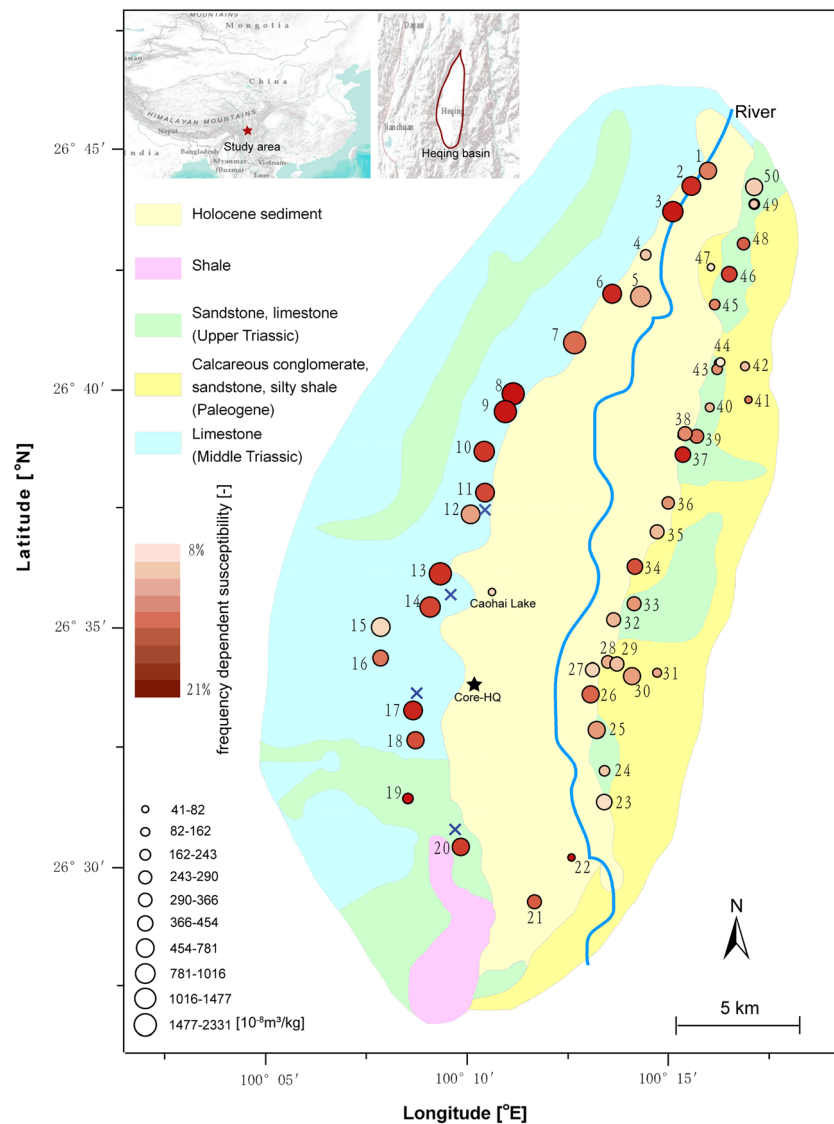


Figure 1. Mass-specific magnetic susceptibility (χ) and percentage frequency dependence of susceptibility ($\chi_{fd}\%$) of red soil samples distributed around the basin (for data see Tables 1 and S1), visualized by circle size (χ) and fill color ($\chi_{fd}\%$). The locations of Core-HQ and Caohai Lake are shown and labeled (referring to site-specific data in Table S1), and sampling sites of limestone bedrock fragments are marked by crosses. Map modified from Hu et al. (2015).

whereas the catchment is less considered. However, knowledge of materials and processes in the source area can provide a better understanding of response mechanisms to paleoclimate conditions and therefore allow better-founded interpretations of lake sediment records.

Heqing Basin (Figure 1) in Yunnan province (SW China) is an example of thick lacustrine sediments deposited in a basin-wide paleolake that existed from 2.78 Ma until subrecent (An et al., 2011; Deng et al., 2019). It represents an important terrestrial archive for studying Indian monsoon evolution in the southeastern margin of the Tibetan Plateau (An et al., 2011; Hu et al., 2015). Hu et al. (2005, 2015) interpreted magnetic properties of a 168-m-deep lacustrine drill core (Core-HQ; Figure 1) in terms of paleoclimate evolution since ~900 ka until the large lake drained at ~30 Ka. They identified magnetite, maghemite, and hematite as the main ferro(i)magnetic components and concluded that the variation in the sediment magnetic properties is mainly controlled by low-temperature oxidation of magnetite (maghemitization) and transformation of magnetite to hematite. Hu et al. (2015) also noted that superparamagnetic (SP) magnetite that dominates the highly magnetic red soil all around the basin is practically absent in Core-HQ. They speculated that

the SP magnetite in the red soil was lost during transport due to dissolution in surface water and concluded that the detrital fraction inherited from the very low-magnetic bedrock in the Heqing Basin catchment dominates the magnetic properties of the lacustrine deposits in Core-HQ.

Red soil is a common soil type in subtropical China (He et al., 2004) and in other subtropical and tropical parts of the world (Bronger & Bruhn-Lobin, 1997; Yaalon, 1997). In China, it developed since the mid-Pleistocene during warm and humid periods (Wang et al., 2013). Highly magnetic red soil is found above strongly magnetic basalt (Liu et al., 2017) but also on low-magnetic sedimentary bedrock (Khadkikar & Basavaiah, 2004; Lu et al., 2012). Magnetic properties of red soil are climate sensitive (Liu et al., 2012; Wang et al., 2013; Yin et al., 2018), and the soil may also serve as an important source material for lake sediment archives as in Heqing Basin. Using magnetic properties as paleoclimate proxies in the context of such scenarios requires an understanding of the formation and characteristics of pedogenic ferro(i)magnetic minerals, as well as subsequent alterations that occur during transport, deposition, and diagenesis.

Heqing Basin is not only a suitable target for investigating the magnetic signature of modern red soil but also for assessing its spatial variability as a function of bedrock lithology and the possible change of magnetic properties during relocation of soil material. As exclusively very low-magnetic bedrock occurs in the Heqing Basin catchment and the highly magnetic soil cover is widely distributed, it is expected that the magnetic properties of lake sediments in the basin are dominated by material derived from red soil. In consideration of the favorable setting, we performed a study in Heqing Basin, investigating in detail the magnetic characteristics and spatial variability of red soil in the catchment and comparing its magnetic signature with subrecent lake sediments of a small modern lake in the basin (Figure 1).

2. Samples and Methods

2.1. Geological Setting and Sampling

Heqing Basin is situated at about 2,200 m above sea level. Present-day climate conditions are subtropical; mean annual temperature and precipitation are 13.5°C and ~1,000 mm, respectively, with strong seasonality in humidity due to monsoon-related major rainfall in the summer months (Xiao et al., 2010). Rock types around the basin (Figure 1), forming the main sources of detritus for lakes in the basin, consist of very low-magnetic limestones at the western side of the basin, sandstone and conglomerates (composed of sandstone and limestone) at the eastern side, and some shales at the southwestern basin margin (Yang et al., 2009). All around Heqing Basin, the bedrock is covered by red soil with thicknesses of some 10 cm to few meters. The red soil is undoubtedly formed in situ as there is a gradual transition of the soil into the bedrock, which is also described for southwestern China in general (Feng et al., 2009). Caohai Lake (26°35'43"N, 100°11'04"E) (lake area 1.8 km²) is the largest of few small modern lakes in the basin, with shallow water depth (~1 to 2 m) and about half meter of sediments. The lake sediments formed above the fluvial sediments that were deposited after the termination of the large Heqing paleolake. According to the positions of Caohai Lake and the Core-HQ drilling site (Figure 1), it is expected that sediments for both Core-HQ and Caohai Lake mainly derived from the limestone terrain at the western basin margin.

We studied samples from the red soil and the Caohai Lake sediments and from the bedrock. In 2016–2019, we collected red soil of the uppermost ~10 cm from a total of 45 sites all around the basin, avoiding possible anthropogenic influence; additionally, we included the results of five samples published by Hu et al. (2015). At three sites at the western basin, we collected soil material from short (5 cm) vertical sections, in particularly discriminating between loose material at the surface (carefully sampled with a soft brush) and underlying compact soil. In addition, we sampled limestone fragments from four sites at the western basin margin (Figure 1). To compare properties of red soil with a sink of red soil material, we recovered three sediment cores from Caohai Lake penetrating through the entire sediment thickness (~0.5 m) using a gravity corer.

In the lab, we cut the cores into subsamples at intervals of 1 cm, then air dried, and sieved the sample material. All red soil and lake sediment samples were placed in 2 × 2 × 2 cm cubic plastic boxes (weighed for determining mass-specific magnetic parameters), which were used for most measurements. For part of the analyses, smaller subsamples were used. Some of the analyses were performed with magnetic extracts. We prepared the extracts by mixing several samples of the same type, sieved the material through a 74-μm wire mesh, stirred it in about 1-L Milli-Q water adding a deflocculant to suppress clumping of clay,

and dispersed the suspension for several minutes in an ultrasonic bath while continuing stirring. Taking about 0.5 L of the obtained suspension and putting it in a magnetic stirrer (HI190M) at ~500 rpm, we performed magnetic separation for about 2 hr, using a separate latex-covered cylindrical magnet (length/diameter 20/12 mm) with relatively weak magnetic moment ($20 \text{ mA}\cdot\text{m}^2$) for extraction. The material was collected several times during this procedure, and before removing the latex cover from the magnet, the extracted material was carefully flushed with Milli-Q water to wash out clay minerals.

2.2. Magnetic Measurements

In the field we used an SM30 sensor (ZH Instruments) to quickly obtain magnetic susceptibility values from the red soil and the bedrock for overview. All laboratory magnetic measurements were carried out at University of Tübingen, Germany, Department of Geosciences. We determined susceptibility with an MFK-1 Kappabridge (Agico), normalized the results to mass-specific values (χ), and calculated the percentage frequency dependence of χ ($\chi_{fd}\%$) by $[(\chi_{lf} - \chi_{hf})/\chi_{lf}] \times 100$ (Dearing et al., 1996), χ_{lf} and χ_{hf} representing readings at frequencies of 976 and 15,616 Hz. Additionally, we measured the broadband-frequency dependence at eight frequencies between 125 and 16 kHz with an SM150L device (ZH Instruments). Using an KLY-3 Kappabridge combined with a CS-3 furnace and a CS-4 cryostat (Agico), we obtained low-temperature and high-temperature thermomagnetic curves of magnetic susceptibility (χ -T curves) for sample masses of ~0.15 g, warming the sample from liquid nitrogen to room temperature and heating it to 700°C in argon atmosphere, respectively.

We obtained anhysteretic remanent magnetizations using a DC-SQUID magnetometer (2G Enterprises) with attached degausser and DC coil, superimposing a 50- μT DC field and a decaying alternating field (max. 100 mT). Subsequently, we imparted an isothermal remanent magnetization (IRM) at a 2-T field with an MMPM9 pulse magnetizer (Magnetic Measurements), which we consider as saturation IRM (SIRM), then applied a 300-mT reverse field ($\text{IRM}_{-0.3\text{T}}$), and calculated the high-coercivity IRM (HIRM) by $[(\text{SIRM} + \text{IRM}_{-0.3\text{T}})/2]$ and an S-ratio by $[1 - \text{IRM}_{-0.3\text{T}}/\text{SIRM}]/2$ (Bloemendal et al., 1992). For selected samples, we obtained detailed IRM acquisition curves with 46 steps up to 2.0 T and applied unmixing with log-normal distributions using the MAX UnMix routine of Maxbauer et al. (2016). For some samples, the SIRM was thermally demagnetized in a TD48 (ASC Scientific) furnace. All IRM intensity measurements were performed with a Minispin spinner magnetometer.

Using small subsamples of ~0.01 g, we obtained hysteresis curves and backfield curves on an PMC MicroMag 2900 AGM (Lake Shore Cryotronics). We analyzed these results in terms of magnetic domain state properties using the Day diagram (Day et al., 1977) and mixing curves of Dunlop (2002). For some samples, we measured first-order reversal curves (FORC) using the MicroMag AGM and processed these results with the software FORCinel (Harrison & Feinberg, 2008).

Moreover, we subjected 10 samples to citrate-bicarbonate-dithionite (CBD) treatment, which removes a large part of fine iron oxide particles in the samples (Hunt et al., 1995). Before the treatment, we gently grinded and sieved the samples through a 74- μm mesh. The further experimental procedure followed the method of Mehra and Jackson (1960) and processing of van Oorschot and Dekkers (1999); a detailed description of the CBD treatment is given in the supporting information. Using ~3–4 g, we measured χ values and χ -T curves of the same sample before and after CBD treatment.

2.3. Nonmagnetic Analyses

We performed high-resolution imaging of the magnetic extracts by transmission electron microscopy (TEM), using a JEOL ARM-200F TEM operated at 200 kV equipped with a cold field emission gun, a CEOS probe corrector for spherical aberrations, and a Gatan Quantum electron energy loss spectrometer (EELS) with DualEELS capability. Samples were prepared by putting droplets from suspension on carbon-coated copper grids. For TEM observation of original red soil, we put material into alcohol, shaking it carefully to avoid changes of the original texture, before taking droplets. Core-loss EELS spectroscopy was used to identify magnetite (or maghemite) and hematite by examining both the core loss peaks and the related energy-loss near-edge structure (ELNES). Spatial elemental mapping was done using spectrum imaging (SI) combining EELS spectroscopy and scanning TEM imaging modes; reciprocal-space information was obtained from both Fourier-transformed high-resolution scanning TEM/TEM images and from diffraction-mode data.

For detecting larger ferro(i)magnetic minerals, we carried out reflected light microscopy (at University of Tübingen, Department of Geosciences) with oil immersion objectives on embedded polished samples prepared from magnetic extracts. For identifying strong magnetic phases, we used ester-based ferrofluid on the sample surface covered with a glass slip.

X-ray diffraction (XRD) analysis of the magnetic extracts was performed using a Bruker D8 ADVANCE Eco diffractometer with a Cu K α tube (40 kV, 25 mA) and an LYNXEYE 1-D SSD160 detector. The samples were measured with an angular range of 5° to 80° 2 θ , an increment of 0.02°, and a measurement time of 1 s per step. Total time of all detector pixels sum up to 160-s measurement time per step 2 θ ; samples used for quantitative analyses were measured until the strongest peak reached at least 40,000 counts. The X-ray powder diffraction data were evaluated using DIFFRAC.EVA V4.2 and Diffrac.TOPAS V5 with an ICSD database. Refined parameters of the Rietveld analysis are background parameters, zero error, sample displacement error, scaling factors, cell parameters, crystallinity, and preferred orientation values of all phases except nano-crystalline kaolinite. The parameters of nano-crystalline kaolinite were refined only in an early stage of the analysis and then fixed to stabilize the optimization process.

Bulk sediment samples were scanned with an Avaatech (GEN-4) X-ray fluorescence (XRF) core scanner, using a Rh anode X-ray tube following the protocol of Kern et al. (2019). Prior to scanning, about 0.5 g of bulk sediment was placed in a Micro X-Cell® and was covered with 4- μ m-thick Ultralene® foil. Measurements were carried out at 10 kV without a filter and a current of 1,000 mA and at 30 kV with a Pd-thick filter and a current of 2,000 mA. Counting time was 30 s, and the slit size was 3 \times 3 mm. Data processing of the X-ray spectra was performed using the bAxilBatch software (Version 1.4, July 2016; www.brightspec.be). Single element counts were normalized to total counts.

To analyze the organic matter content, the loss on ignition (LOI) method after Dean (1974) and Bengtsson (1986) was applied, in which weight loss is measured after heating. About 1 g of homogenized dry material was put in crucibles and heated in a ROHDE TC304 muffle furnace at 550°C for 4 hr to combust organic matter to ash and CO₂ (Heiri et al., 2001). From the dry weights before and after the combustion (DW and DW₅₅₀), the LOI₅₅₀ is obtained by $100 \times (DW - DW_{550})/DW$ (Heiri et al., 2001).

For two red soil and three lake sediment sample sets (mixed from several samples), we determined the content of dissolved organic carbon with a total organic carbon (TOC) analyzer (Elementar, highTOC II, version “L”) and the inorganic carbonate (CaCO₃) by titration with NaOH, after digestion with 0.8% HCl.

The TEM studies were carried out at the NMI Reutlingen; XRD, XRF, and LOI analyses were done at Heidelberg University, Germany (Institute of Earth Sciences); organic and inorganic carbon contents were measured at University of Tübingen, Germany (Department of Geosciences).

3. Results

The experimental results comprise the identification of ferro(i)magnetic minerals (section 3.1), their grain size and magnetic domain state (section 3.2), and the determination of the spatial (red soil) and vertical (lake sediments) variabilities of magnetic parameters (section 3.3). Means and standard deviations are listed in Table 1, and for detailed sample results, see Tables S1–S7.

3.1. Magnetic Mineralogy

χ -T curves (Figure 2a) allow the identification of ferro(i)magnetic phases by their Curie temperature and other typical phase transitions. The measured high-temperature χ -T runs are partly compromised by the formation of new magnetite starting around 400–450°C during heating. Despite this effect, the shape of the heating curves together with the single Curie temperature observed at ~580°C proves the existence of magnetite in both the original red soil and lake sediment materials. The low-temperature χ -T dependence does not show the Verwey transition of magnetite. Nonstoichiometry induced by low-temperature oxidation is known to suppress this transition at an already low degree of oxidation (Aragón et al., 1985).

A striking feature of the red soil results is the increase of χ values between –196°C and ~250°C with a hump and subsequent decrease. This effect is also seen in the χ -T curves of the lake sediments, however, less pronounced. At a first glance, partial heating-cooling curves (Figure S1) to subsequently increasing maximum temperatures of about 210°C, 250°C, and 280°C look irreversible and seem to indicate destruction of

Table 1
Mean Values With Standard Deviations for Magnetic Parameters From Red Soil and Lake Sediments

Parameters	Units	Red soil W	Red soil E	Caohai sediments
χ	$(10^{-8} \text{ m}^3/\text{kg})$	1085.3 \pm 579.5	302.0 \pm 160.4	41.0 \pm 15.1
χ_{fd}	(%)	17.8 \pm 3.0	15.1 \pm 3.1	10.6 \pm 2.5
		(N = 17)	(N = 28)	(N = 44)
SIRM	$(10^{-3} \text{ Am}^2/\text{kg})$	38.8 \pm 17.6	18.3 \pm 10.7	3.7 \pm 1.1
HIRM	$(10^{-5} \text{ Am}^2/\text{kg})$	84.2 \pm 62.3	110.4 \pm 85.8	35.8 \pm 11.7
S ratio	(-)	0.98 \pm 0.02	0.93 \pm 0.07	0.9 \pm 0.02
SIRM/ χ	(kA/m)	4.2 \pm 1.6	6.5 \pm 3.1	9.4 \pm 1.1
HIRM/ χ	(kA/m)	0.12 \pm 0.13	0.58 \pm 0.92	0.94 \pm 0.26
		(N = 17)	(N = 27)	(N = 13)
M_{rs}/M_s	(-)	0.18 \pm 0.01	0.20 \pm 0.05	0.20 \pm 0.04
H_{cr}/H_c	(-)	2.82 \pm 0.30	2.61 \pm 0.45	2.47 \pm 0.24

Note. For definition of parameters, see section 2.2. N = number of samples included. Red soil separated into western and eastern basin sides. For detailed sample results, see Tables S1–S3.

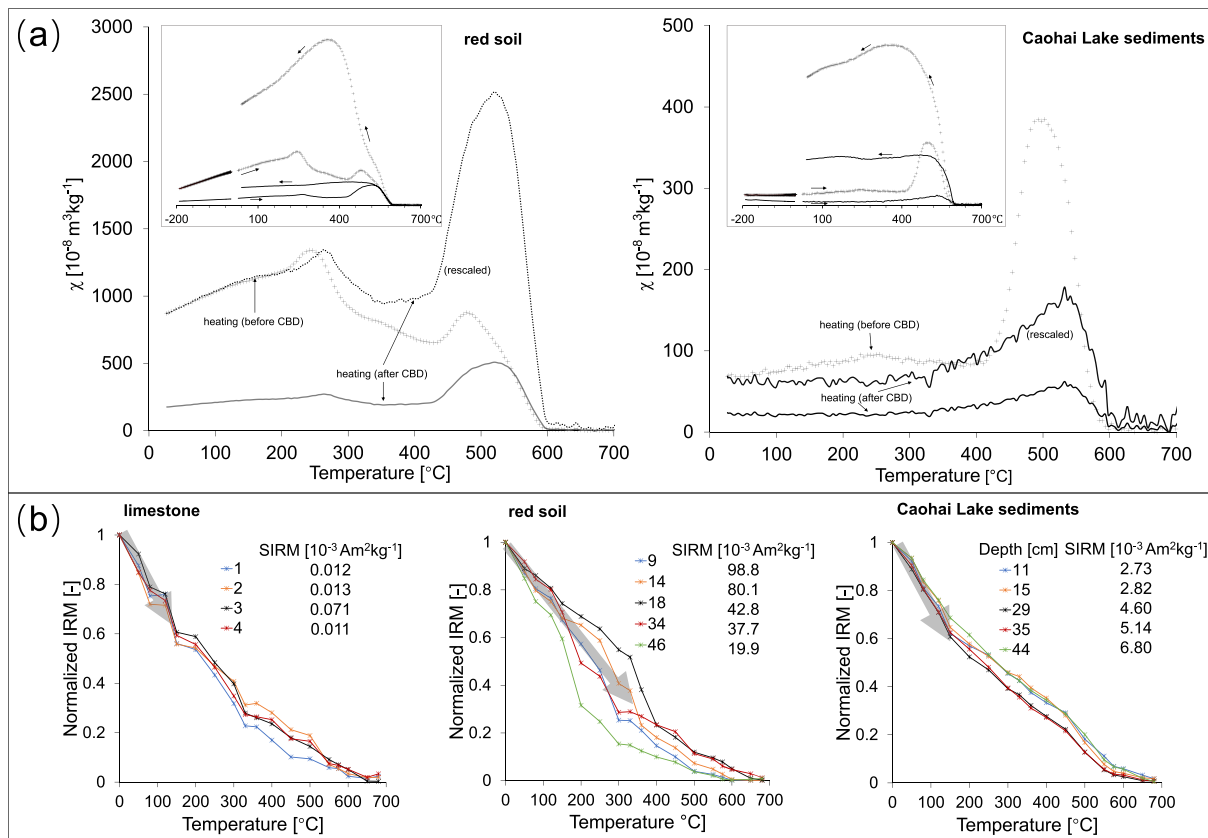


Figure 2. (a) χ -T curves for red soil and Caohai Lake sediments (out of five measured samples for each) of magnetic susceptibility (χ) before and after citrate-bicarbonate-dithionite (CBD) treatment and (b) SIRM thermal demagnetization (all measured samples) for limestone, red soil, and Caohai Lake sediments (starting values of SIRM are listed and labeled; for red soil numbers relate to sites in Figure 1, for the lake sediments numbers are depth levels). Large plots in (a) show heating curves with absolute χ values (bold curves); rescaled curves are post-CBD results normalized to the starting value of the pre-CBD curves (allowing better comparison of their shapes); the smaller plots in (a) show heating and cooling runs, together with low-temperature χ -T results; partial heating-cooling curves for red soil are shown in Figure S1. Gray arrows in (b) indicate pronounced IRM intensity loss.

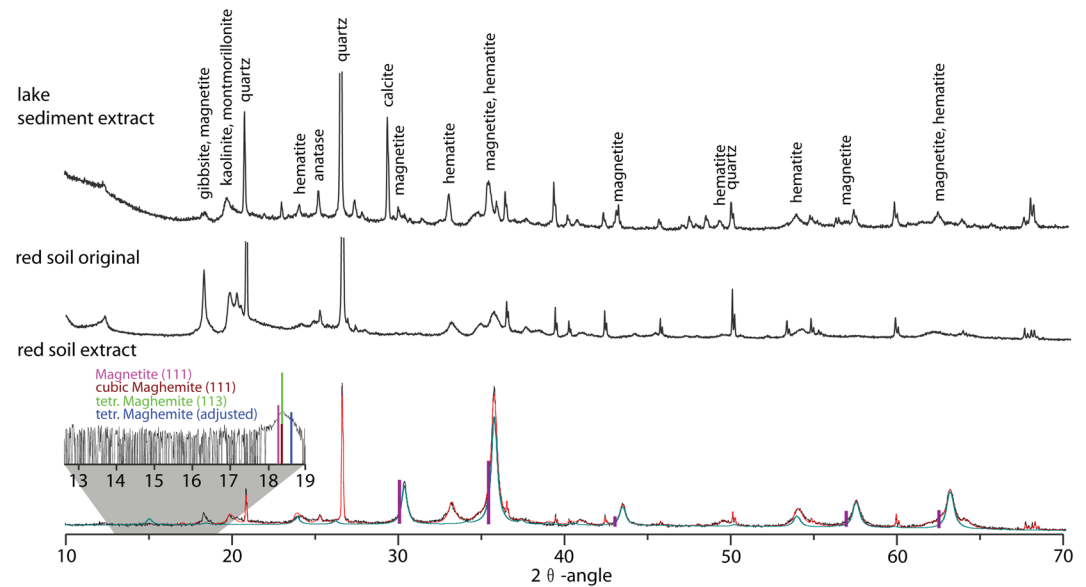


Figure 3. X-ray diffractograms of original red soil and for magnetic extracts of red soil and Caohai Lake sediments. Main peaks are labeled. For the red soil extract, a Rietveld model for 49.2 vol.% nano-maghemite (16 nm size; $a = 0.833$ nm according to Pecharrómán et al., 1995) is shown (green diffractogram). The entire model diffractogram (red) fitting the measured diffractogram involves the nano-maghemite, 12.6% quartz, 15.8% hematite, 8.1% Illite, 10.9% kaolinite, 2.1% muscovite, and 1.4% anatase (all values vol.%). Purple bars show the expected positions of magnetite peaks ($a = 0.8397$ nm according to O'Neill & Dollase, 1994). The inset plot above the red soil extract diffractogram shows a high-resolution measurement of this material for the 2θ range of $12.5\text{--}19^\circ$; vertical bars mark the position of theoretical magnetite and maghemite peaks. From the XRD result of the original red soil, the hematite ($a = 0.5026$ nm, $c = 1.377$ nm, cell volume 0.3013 nm³) content is estimated at ~ 5 vol.%.

maghemite during heating as it is often argued in literature (Bilardello & IRM, 2020). In fact, this might be the case. Remarkably, the χ values in the cooling curves of the first two runs return to about the starting value before heating, which is incompatible with maghemite destruction. The increase and hump could be alternatively explained by fine magnetite particles, which show a typical maximum-type χ -T dependence when transforming from stable single domain (SSD) to the SP state (see review in Bowles et al., 2009). For magnetite, the SP-SSD transition is at ~ 25 nm (Worm, 1998). A broad hump will result from superposition of fine magnetite particles with different grain sizes and therefore different SSD-SP transition temperatures. We interpret the apparent irreversible behavior in the χ -T curves as thermal hysteresis residing in fine-particle behavior, which, so far, seems unrecognized in rock magnetism, however, such kind of magnetocaloric effects are reported in literature related to technical applications (Souza et al., 2019). After the CBD treatment, which destroyed a large fraction of fine magnetite particles (but not all), the hump is less distinct for red soil and no more detectable for lake sediments.

A distinctly stronger drop of the remanence intensity close to 580°C in thermal demagnetization curves of SIRM (Figure 2b) suggests the presence of magnetite in all samples, including the limestone bedrock despite its weak SIRM. Moreover, the presence of hematite is evidenced for all measured lake sediment samples and part of the red soil samples, shown by a residual remanence beyond 580°C that is demagnetized until 700°C .

XRD results for magnetic extracts from both red soil and lake sediment materials confirm the presence of magnetite and hematite (Figure 3). The diffraction peaks are shifted to larger 2θ angles than expected for stoichiometric magnetite, corresponding to a lattice constant of 0.833 nm (Rietveld analysis of the red soil extract), which indicates a strong degree of maghemitization (Readman & O'Reilly, 1972). The strong degree of maghemitization, as documented by the XRD results of the red soil sediment material, implies a transition process from magnetite to (potentially tetragonal) maghemite, which we will further discuss in section 4.1. The XRD result of the original red soil allows to estimate the content of hematite (~ 5 vol.%), while magnetite is below the detection limit. The hematite peaks are close to pure $\alpha\text{-Fe}_2\text{O}_3$, which means that Al-substituted hematite that is often found in soil (Jiang et al., 2012) is of minor importance in our samples. The cell volume (0.3013 nm³) determined from the Rietveld fit corresponds to an Al_2O_3 content of 1–3 vol.% according to the

cell parameters of Feenstra et al. (2005) for $\text{Fe}_2\text{O}_3\text{-Al}_2\text{O}_3$ solid solutions. The mineral assemblages revealed by the XRD results show obvious similarities between red soil and lake sediment materials, indicating that there is a notable relationship between them. A difference is a strong XRD signal of calcite for the lake sediment extract, which is not appearing in the red soil result. Chemical analysis of inorganic carbonate yielded a much higher content in the lake sediment (~25 wt.%) compared to red soil (4–5 wt.%), which hints at a large amount of calcite that was directly transferred from weathered limestones to the lake, either by detrital input or authigenic precipitation of dissolved carbonate.

3.2. Grain Size of the Magnetite Fraction

The width of the magnetite (maghemite) diffraction peaks was modeled by a Rietveld fit (Figure 3) using a crystal size of 16 nm (cube shaped). Direct measure of the physical grain size results from TEM observations and optical microscopy. In the first set of TEM analyses, we used magnetic extracts with an enrichment of magnetite to roughly 10–15 wt.% (estimated from χ values).

TEM images (Figures 4 and 5) reveal the presence of numerous up to >100-nm large aggregates of ultrafine particles with individual sizes of ~5–20 nm (mostly ~10–15 nm). High-resolution TEM images (Figures 4d and 5c) show coherent lattice structures across ~10- to 15-nm dimension. ELNES point analysis along line scans (Figures 4b, 4c, and 5b) with a beam width of ~5 nm allows the discrimination between magnetite (or maghemite) and hematite by the existence (in case of magnetite or maghemite) or absence (in case of hematite) of a small peak or shoulder (marked by dashed boxes in Figures 4e and 5d) in the O K-edge (Colliex et al., 1991; Golla-Schindler et al., 2006). We found that ELNES results are more useful for discrimination between magnetite/maghemite and hematite than power spectra of Fourier transforms because the determinative lattice spacings are not necessarily present in any particular high-resolution image due to orientation, and many reciprocal-space lattice spacings are similar between the materials. The ELNES characteristics of the red soil (Figure 4e) clearly reveal magnetite (or maghemite) in the nanoparticles of the aggregates, and variable expression of the sensitive peak/shoulder indicates that some spots represent a significant contribution of hematite. Likewise, the nanoparticles in the aggregates of the lake sediments show ELNES patterns (Figure 5d) typical for magnetite (or maghemite) and hematite. The discrimination between magnetite (or maghemite) and hematite is less clear than for the red soil sample, indicating a larger contribution of hematite than in red soil.

Results of reflected light microscopy (Figures 4f and 5e) prove the additional presence of large detrital magnetite particles with grain sizes up to several tens of micrometer. Surfaces with ferrofluid provide unambiguous evidence strong magnetic particles, and these particles could be identified as magnetite or maghemite by the appearance of magnetite-ilmenite exsolution structures and an isotropic behavior in crossed polarizers. Besides the magnetite (maghemite), oxidation to hematite (martitization) is observed in surface areas not covered by ferrofluid (optically anisotropic).

In order to check whether the aggregates of magnetite nanoparticles were formed by clumping during the magnetic extraction process, we performed a further TEM analysis using the original red soil material. No noteworthy differences between original red soil and magnetic extracts from red soil were found in the appearance of the aggregates (Figure 6a). Within the aggregates, it is hard to distinguish individual particles, except through lattice fringes. High-resolution TEM images (Figures 6b and 6c) indicate that lattice fringes are not aligned, suggesting that the particles did not grow epitaxially. Around the aggregates, we found splattered smaller crystalline particles (Figure 6d), which are typically thinner in the interior than at the rim (identified by high-angle annular dark-field scanning mode). This observation might indicate that some parts of the aggregates fell apart. Such donut-like shapes unlikely represent minimum-energy structures, which means they did not form as separate nanoparticles. Moreover, if the aggregates were formed during sample preparation, then particle splatter away from the aggregates too should be seen. Because of these observations, clumping of the magnetite nanoparticles during magnetic extraction or any other sample preparation process is unlikely, but the opposite, that is, breakup of aggregates, might be the case.

After CBD treatment, the χ values at room temperature decreased on average by 70.6% for red soil and 55.1% for lake sediments (Table S4). The CBD procedure efficiently dissolves fine magnetite particles smaller than about 1 μm , while larger particles are much less affected because of their smaller surface-to-volume ratio (Hunt et al., 1995). After CBD treatment, the hump in the χ -T curves is still clearer for red soil than for

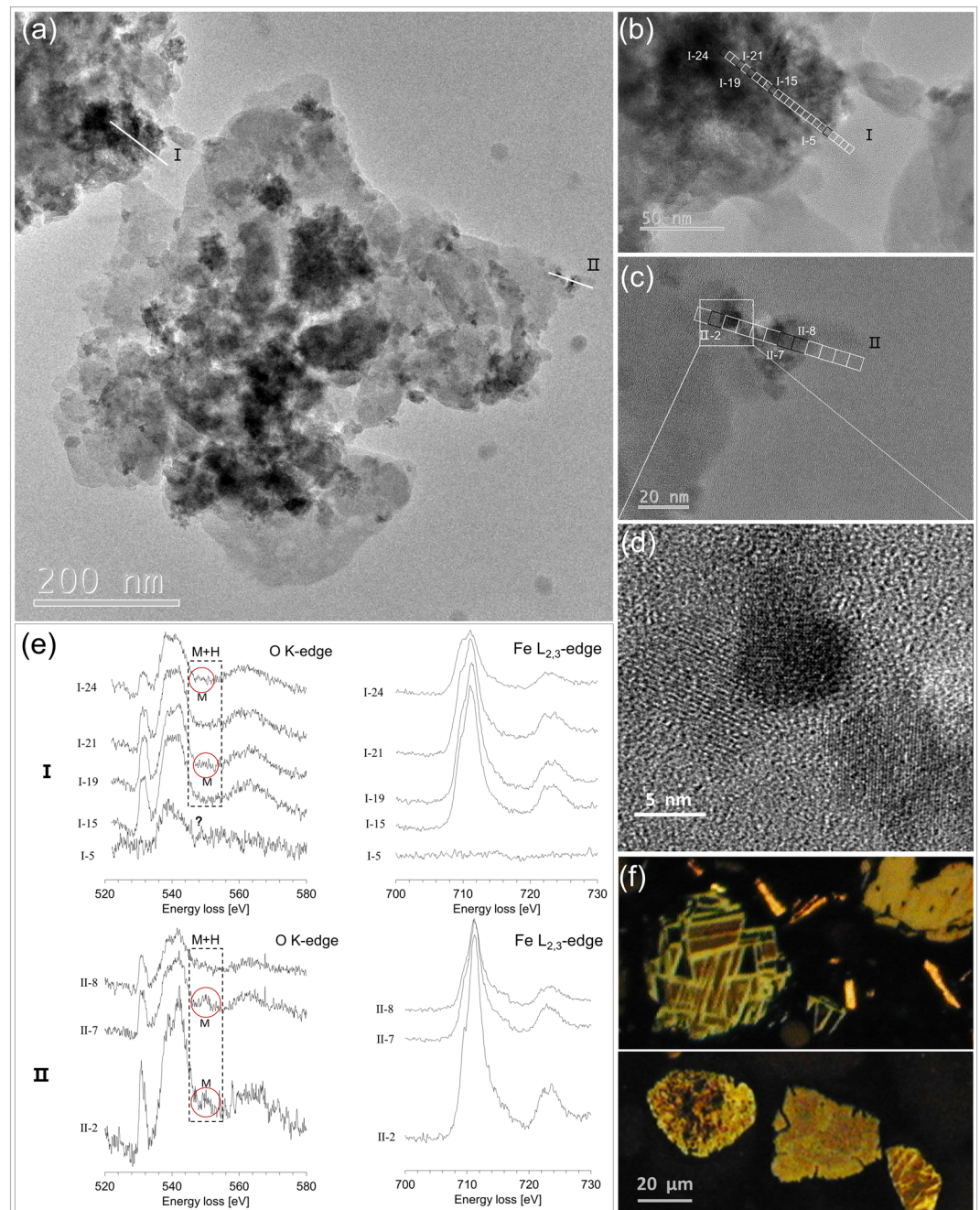


Figure 4. TEM images of the magnetic extract from red soil (a) with enlargements (b, c), showing aggregates of nanoparticles. The HRTEM image (d) shows coherency of lattice structures across ~ 10 nm. In (e), ELNES results of the O K-edge and Fe $L_{2,3}$ -edge structures are shown for selected spots (marked in b, c) along two traverses (marked in a–c), identifying magnetite or maghemite (M) by a peak or shoulder in the O K-edge (clear magnetite-maghemite signals are marked by red circles within the dashed box); the additional contribution of hematite (H) is indicated by the variable expression of the peak. Unclear interpretation or absence of Fe-oxides is marked by “?”. All other measured ELNES spectra from red soil are shown in Figures S2 and S3. Reflected light microscopy images in (f) show several 10- μm large detrital magnetite particles (the dark brown ferrofluid cover evidences strong magnetic phases).

the lake sediments, which together with the larger decrease of χ values indicates a higher proportion of fine magnetite particles in red soil. This is further confirmed by the $\chi_{fd}\%$ values before and after CBD treatment (Table S4), which are quite stable for red soil (decrease of the mean from 18.5% to 18.3%) and decrease substantially for the lake sediments (from 12.9% to 5.2%). The CBD treatment dissolves SP particles

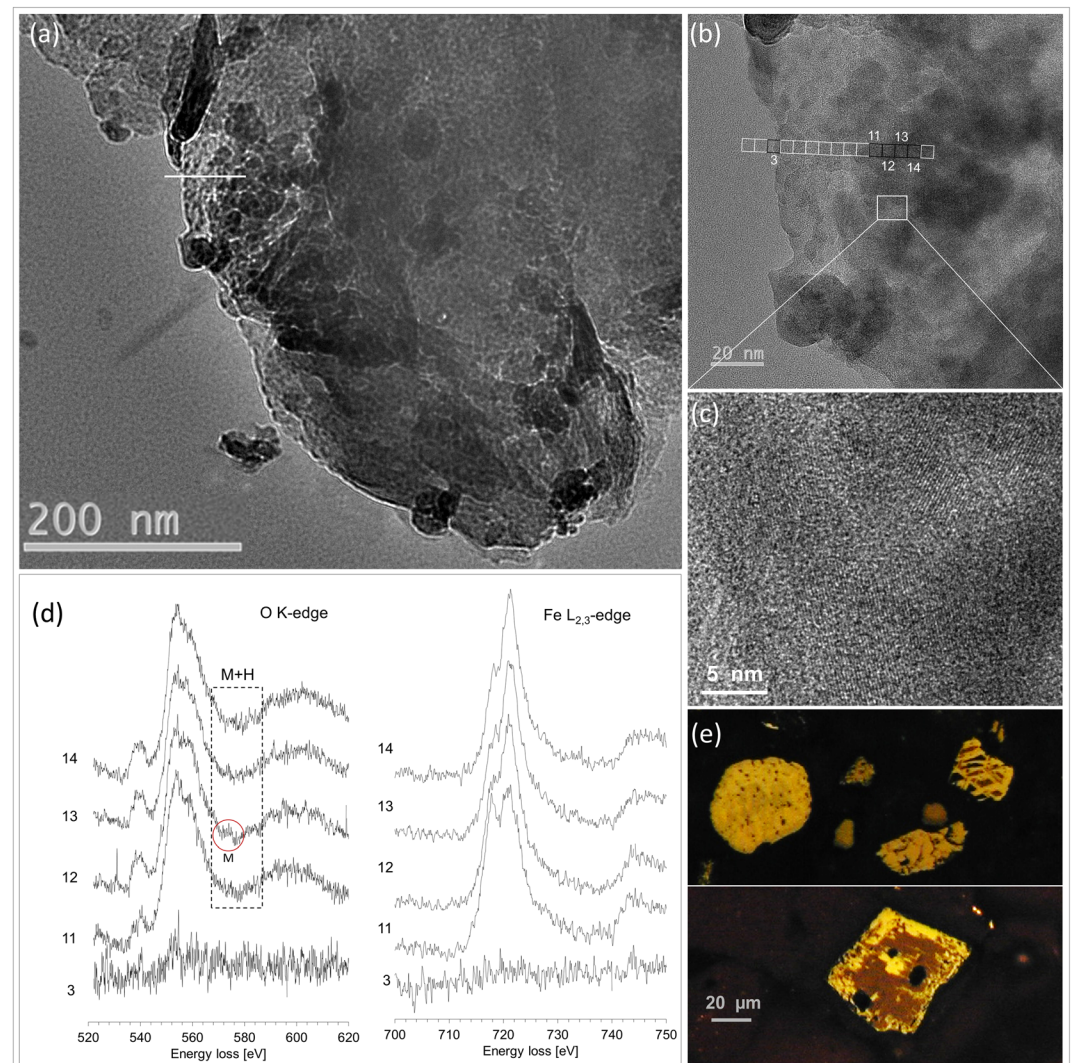


Figure 5. TEM images of the magnetic extract from lake sediments (a) with and enlargement (b), showing aggregates of nanoparticles. The HRTEM image (c) shows coherency of lattice structures across ~ 10 nm. In (d), ELNES results of the O K-edge and Fe $L_{2,3}$ -edge structures are shown for selected spots (marked in a, b), identifying magnetite or maghemite (M) and by a peak or shoulder in the O K-edge (clear magnetite-maghemite signals are marked by red circles within the dashed box); the additional contribution of hematite (H) is indicated by the variable expression of the peak. Unclear interpretation or absence of Fe oxides is marked by "?". The EELS spectrometer was operated to capture two simultaneous core losses in dual-EELS mode, thus the exact energy offset was not recorded and energy offsets between 6d and Figure 4e are not interpretable. All other measured ELNES spectra from lake sediments are shown in Figure S4. Reflected light microscopy images in (e) show several $10\text{-}\mu\text{m}$ large detrital magnetite particles (the dark brown ferrofluid cover evidences strong magnetic phases).

efficiently, but not completely. According to the χ decrease, about approximately one third of the magnetite is still existing in the red soil after CBD treatment, and the rather unchanged $\chi_{fd}\%$ proves that SP grains are still highly predominant after the CBD treatment. This means that larger multidomain (MD) magnetite grains inherited from the bedrock contribute only very little to the total magnetite content in the red soil. In the lake sediments, where the χ decrease after CBD treatment is less and $\chi_{fd}\%$ decreases significantly, the relative χ proportion of SP magnetite compared to bedrock-derived larger grains is clearly lower than in red soil.

The broadband-frequency results of χ between 125 and 16,000 Hz show a decrease of χ with frequency (f) (Figure 7 and Table S5) as expected for SP behavior. The shape of the $\chi(f)$ dependence is related to the specific grain-size distribution of particles in the SP range, with larger SP particles showing a stronger $\chi(f)$ decrease at

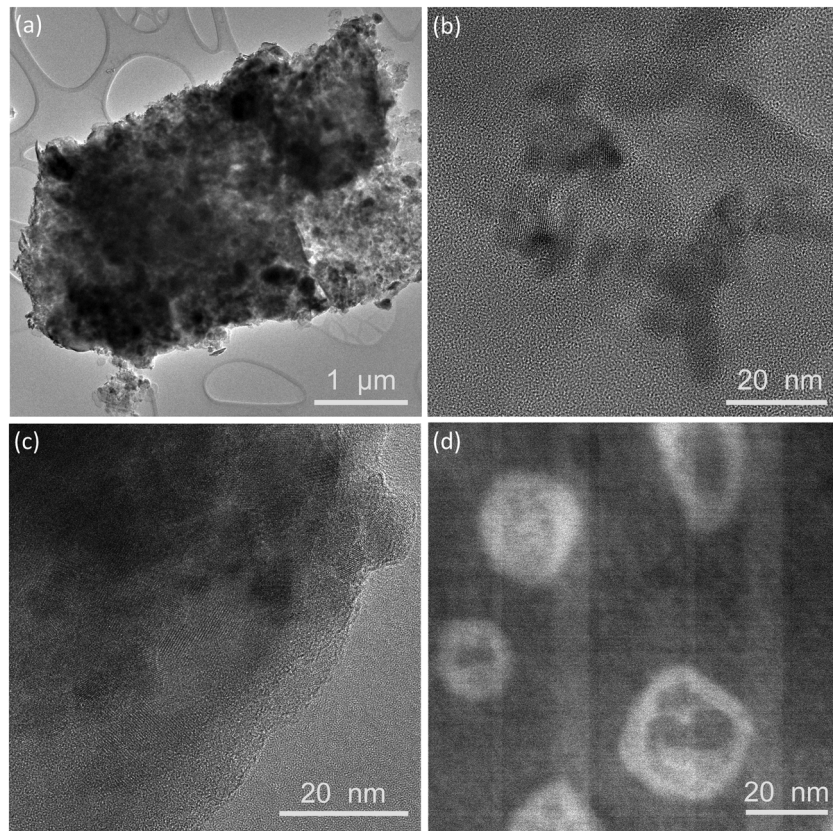


Figure 6. (a) TEM image of original red soil showing an overview of a sample patch with different particles, including numerous aggregates of nanoparticles. (b, c) HRTEM images of nanoparticle aggregates. The image in (d) obtained in high-angle annular dark-field scanning mode shows donut-like nanoparticles with thicker rims (lighter) and thinner interior, which were found splattering around aggregates.

lower frequencies and vice versa (Kodama, 2013). It is obvious that the χ -log(f) dependence of the lake sediment samples with lower susceptibility (lake sediments L) flattens in the lower-frequency range. Calculating regression lines separately for the lower-frequency (0.125–1 kHz) and higher-frequency (1–16 kHz) parts allows a quantitative assessment of the χ -log(f) slopes in the two frequency ranges. For the red soil H samples, the slope at 0.125–1 kHz is slightly steeper than at 1–16 kHz. For the lake sediments L, it is the opposite, and the slopes at 0.125–1 and 1–16 kHz are different at a 95% confidence level (for statistical results, see Table S6). This indicates a loss of SP behavior in the larger SP grain size range for the lake sediments, which we will elaborate further in the discussion.

The IRM results provide information about the ferro(i)magnetic fraction in the SSD to MD state. During thermal demagnetization, most of the remanence intensity is lost far below the Curie temperature of magnetite (Figure 2b). This lower-temperature loss is much stronger in red soil than in lake sediments (indicated by gray arrows in Figure 2b). The decay of SIRM at low to medium temperatures likely reflects remanence unblocking of fine magnetite particles when they undergo the SSD-SP transition. This is in line with the interpretation of the hump in the χ - T curves (Figure 2a) in terms of fine-particle behavior and with the IRM unmixing results (Figure S5). Values of B_h for the lower coercivity component range from few mT to several 10 mT. The lowermost B_h values can be related to magnetite particles at the transition from SSD to SP, and the relatively higher B_h values indicate magnetite with SSD behavior and/or larger magnetite particles in the MD range (which cannot be discriminated by IRM unmixing). For the limestone samples, only the relatively higher coercivity fraction is observed.

In the Day diagram, the data of the red soil and lake sediment samples plot in a region of mixed SP, SSD, and MD particles (Figure S6). Despite the criticism on the significance of the Day plot (Roberts et al., 2018), we think that the results can be considered as a rough estimate of similar portions of SSD and MD, plus a

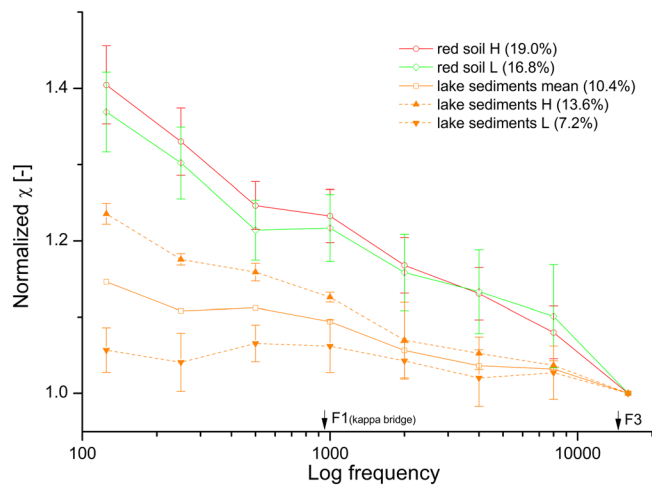


Figure 7. Broadband-frequency dependence of magnetic susceptibility for red soil (red = samples with $\chi > 10^{-5} \text{ m}^3/\text{kg}$; green: samples with $\chi < 10^{-5} \text{ m}^3/\text{kg}$; 10 samples each) and Caohai Lake sediments (orange; broken curves represent samples with higher-H and lower-L χ values taken from 31- to 35- and 9- to 13-cm depths, respectively; the full curve shows the means of both). For the full curves, the mean values represent an average of 10 samples; for the broken curves, the mean is obtained from five samples. The χ values were first normalized by their 16-kHz value, and then means and standard deviations of the normalized values were calculated (thus the 16-kHz value has no standard deviation). The two frequencies used for the MFK-1 for determining ($\chi_{fd}\%$) of bulk samples are marked (F1, F3), and mean values of $\chi_{fd}\%$ for the used samples are listed in the legend (in brackets). For detailed data, see Table S5.

substantial SP contribution. The red soil samples from the western basin deviate most from the SSD-MD mixing line toward an increasingly larger SP contribution. The lake sediments plot closest to the SSD-MD mixing line indicating a relatively lower SP proportion. FORC diagrams (Figure S6) support a wide grain size range of the fine magnetite fraction, but a conclusive comparison of red soil and lake sediments is not possible because the latter are too weakly magnetic to obtain meaningful FORC results without magnetic extraction.

3.3. Spatial and Vertical Magnetic Parameter Distribution of Red Soil and Lake Sediments

An overview of the spatial distribution of χ and $\chi_{fd}\%$ for red soil is shown in Figure 1. Means and standard deviations are listed in Table 1 (site-specific data in Table S1), together with other parameters. All red soil samples show high χ values, higher above the limestone bedrock at the western basin (ranging from 216×10^{-8} to $2,331 \times 10^{-8} \text{ m}^3/\text{kg}$, mean of $1,085 \times 10^{-8} \text{ m}^3/\text{kg}$) than above conglomerates and sandstones at the eastern basin (ranging from 60×10^{-8} to $751 \times 10^{-8} \text{ m}^3/\text{kg}$, mean of $302 \times 10^{-8} \text{ m}^3/\text{kg}$). Values of $\chi_{fd}\%$ are much less different between the western (mean of 17.8%) and eastern (mean of 15.1%) sides of the basin.

The samples from the short surface-near-vertical profiles taken at three sites were studied to check for possible differences between loose material at the surface (carefully sampled with a soft brush) and the underlying 5–6 cm of red soil. The χ values of the surface samples and deeper levels do not differ systematically, and the differences are within the range of surface χ variations measured in situ within an area of few m^2 (Figures S7a and S7b). Likewise, $\chi_{fd}\%$ values do not show a clear difference (Figure S7a).

Magnetic data and geochemical data of the Caohai Lake sediments versus depth are shown in Figure 8 and listed in Table 1 (for data, see Table S2). Part of the magnetic parameter means from red soil is also plotted in Figure 8 for comparison. Compared to the red soil, the χ values of the lake sediments are much lower (ranging from 20×10^{-8} to $61 \times 10^{-8} \text{ m}^3/\text{kg}$, mean of $41 \times 10^{-8} \text{ m}^3/\text{kg}$). They show an increase from ~15 cm downward and reach about twice as high values compared to the top part at ~30 cm. Values of $\chi_{fd}\%$ are between 6.2% and 14.2% (mean of 10.6%), with downward increasing trend. The SIRM is relatively stable in the upper ~15 cm, increases gradually by a factor of about 2 at ~15–40 cm, and then shows a strong increase in the lowermost ~5 cm. The HIRM is only slightly increasing downward to ~40 cm and then doubles within the lowermost ~5 cm.

The XRF data show two distinctive features in the downcore sediment geochemistry, that is, a gradual increase in the Fe/Mn ratio toward the top of the sequence and pronounced increases in the Fe/Ti and Si/Ti ratios, and the S and Br counts in the uppermost 10 cm, with a drop of these values for the top-most samples, in particular for Fe/Mn, S, and Br. The LOI that is a proxy of the organic carbon content follows the vertical trend of the various XRF results also shows a distinctive drop at the top. Organic carbon analyses of mixed samples from three different depth intervals confirm the trend of the LOI values (Figure 8). The organic carbon contents range between 2.2 and 5.0 wt.%, which is relatively low for lake sediments and not much higher than in the red soil (2.1 and 3.4 wt.% for two samples analyzed). From comparison of data in Figure 8, we notice that the increase of the geochemical parameters occurs at a clearly shallower depth as for the magnetic parameters χ and $\chi_{fd}\%$. In the discussion, we will assess the relationship of magnetic and geochemical in terms of possible solution of Fe oxides based on the significance of the geochemical parameters for reductive conditions.

4. Discussion

In the discussion, we focus on the following aspects: (i) the nature of ferro(i)magnetic minerals in the red soil and the Caohai Lake sediments; (ii) the spatial variability of magnetic parameters of modern red soil in

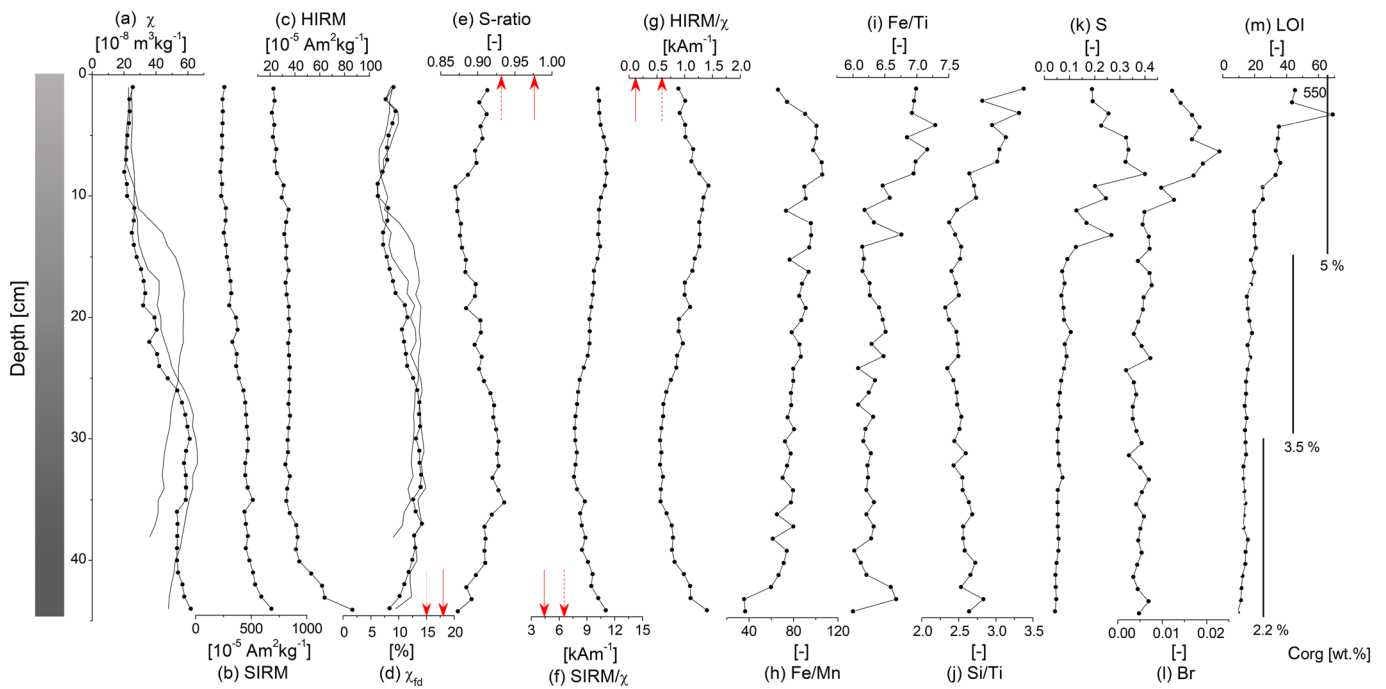


Figure 8. Magnetic and geochemical parameter variations versus depth for the Caohai Lake sediments: (a) magnetic susceptibility (χ); (b) saturation isothermal remanence (SIRM); (c) hard isothermal remanence (HIRM); (d) percentage frequency dependence of χ ($\chi_{fd}\%$); (e) S ratio; (f) SIRM/ χ ratio; (g) HIRM/ χ ratio; (h) iron/manganese (Fe/Mn) ratio; (i) iron/titanium (Fe/Ti) ratio; (j) silicon/titanium (Si/Ti) ratio; (k, l) relative contents of sulfur (S) and bromine (Br); and (m) loss of ignition at 550°C (LOI) and wt.% of organic carbon content for three mixed samples. Curves in (a) and (d) without symbols show data from two additional cores for consistency check. In (d)–(g), magnetic parameter means of red soil at the western and eastern basin are shown by red full and dashed arrows, respectively, for comparison. For concentration-dependent parameters (a–c), see Tables 1 and S2. The column at the left side indicates that the sediment color is getting darker downcore.

Heqing Basin in order to identify possible environmental proxies; (iii) characteristic differences of magnetic properties of the red soil and the Caohai Lake sediments with regard to changes during transfer from in situ to the sink (lake sediments); and (iv) relevance of the results for using magnetic properties as paleoclimate proxies in settings as studied.

According to the presented results, the studied samples contain magnetite with different degree of maghemitization. The resulting assemblages of particles may range from near-stoichiometric magnetite to fully altered maghemite, which we interpret to reflect a causal relationship of alteration. For the sake of simplicity, we will speak of “magnetite” in the further course of the discussion when interpreting the results in principle, unless the difference between magnetite and maghemitized magnetite plays an important role.

4.1. Magnetic Characteristics of Red Soil Versus Lake Sediments

In previous works, magnetic signals in modern soils and paleosols were mainly ascribed to pedogenic formation of magnetite or maghemite in the SP and SSD range, with χ values ranging up to $\sim 500 \times 10^{-8} \text{ m}^3/\text{kg}$, mostly centered around $100 \times 10^{-8} \text{ m}^3/\text{kg}$ (Dearing et al., 1996; Deng et al., 2004; Maher, 1998; Song et al., 2014). An exceptionally large amount of fine magnetite in the SP range was observed throughout an $\sim 7\text{-m}$ -thick section of red soil above low-magnetic calcareous rock in southwest China, with the highest χ values (up to $\sim 6,000 \times 10^{-8} \text{ m}^3/\text{kg}$) ever reported in soil (Lu et al., 2012). Khadkikar and Basavaiah (2004) also observed high values up to $\sim 1,000 \times 10^{-8} \text{ m}^3/\text{kg}$ for modern red soil on karst terrain in India, however, with surprisingly low $\chi_{fd}\%$ of around 2% that cannot be explained by the specific frequencies of the used instrument (Bartington MS2B). The χ enhancement in the red soil of Heqing Basin is approximately similar to these previous studies of red soil.

In Heqing Basin, the highly magnetic red soil above low magnetic bedrock occurs on large spatial scale. It contains magnetite and hematite, as verified by XRD results (Figure 3), ELNES spectra (Figures 4d and 5c), and χ -T curves. Their molar contents are roughly ~ 0.5 and $\sim 5 \text{ vol.}\%$ for magnetite (estimated from χ

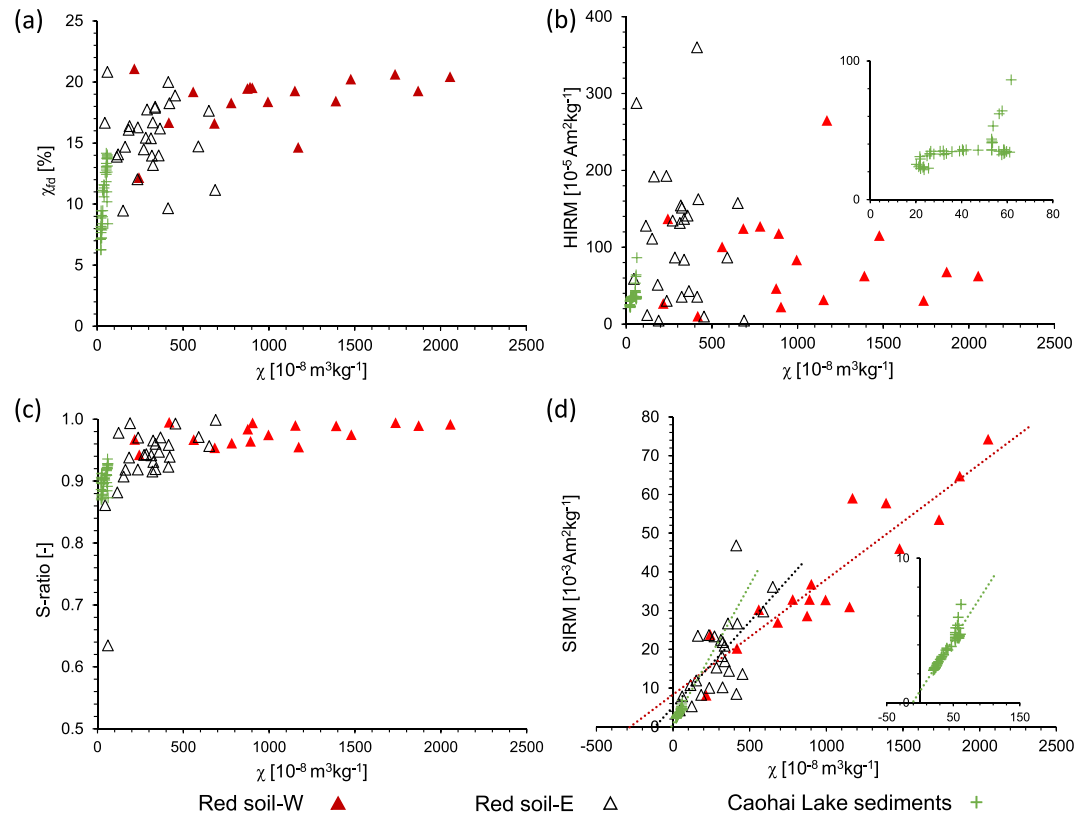


Figure 9. Magnetic parameters plotted versus magnetic susceptibility (χ). (a) χ_{fd} %, (b) HIRM, (c) S ratio, and (d) SIRM. Data are separated for red soil at the western and eastern basins and Caohai Lake sediments. Dotted lines in (d) show linear regressions of the three sub-data sets. The small plots in (b) and (d) amplify the results of the lake sediments.

and M_s) and hematite (estimated from XRD results and HIRM), respectively. The extremely asymmetric 2θ peak at 18.4° in the XRD results (Figure 3) suggests a mixture of maghemitized magnetite with a cubic structure and a tetragonal superstructure (Bowles et al., 2011), which would explain the small lattice constant observed by Rietveld refinements using magnetite structures. The intensity maximum of this peak fits to magnetite, cubic maghemite, and synthetic maghemite. If the tetragonal maghemite cell is adjusted to the shoulder of the 18.4° 2θ peak, the Position 102 and the 112 peak move to areas where no peaks are measured. This observation may fit to cubic maghemites which suffer a higher loss of iron that may change the structure from cubic to tetragonal. The observed material seems to be in a transitional state between both structures or it contains oxides of both structures. The mixture would also explain the extremely small cell constants observed by Rietveld refinements using magnetite structures. The value of the maximum intensity at the 18.4° 2θ peak is located in the known range of common magnetite or maghemites.

The generally high χ_{fd} % of the red soil (~ 15 – 18% ; Table 1), together with the almost stable χ_{fd} % after CBD treatment (Table S4), prove a strong dominance of fine magnetite in the SP range, even in samples with relatively lower magnetic concentrations as shown by χ_{fd} % values $>15\%$ for χ values above several hundred $10^{-8} \text{ m}^3/\text{kg}$ (Figure 9a). The SP fraction hides the presence of larger-sized bedrock-derived MD magnetite that is revealed by reflected light microscopy. The results of χ -T behavior, broadband-frequency dependence $\chi(f)$, thermal demagnetization of SIRM, IRM-unmixing, and data distribution in the Day plot all together suggest that the fine magnetite fraction occurs in a wide grain size distribution of SP particles that also tails into the SSD range. The presence of magnetite nanoparticles with sizes from <10 to about 20 nm , mostly occurring in aggregates of up to $\sim 100 \text{ nm}$, is clearly evidenced by the TEM results (Figures 4–6).

From the values of χ and M_s , we can roughly estimate the magnetite content. Because of its very high intrinsic susceptibility, the measured χ value is a function of the inverse of the demagnetization factor (N) and the magnetite content. Assuming spherical single domain particles ($N = 1/3 \text{ SI}$), the mean χ value of the red soil

at the western basin ($1,085 \times 10^{-8} \text{ m}^3/\text{kg}$) corresponds to ~ 0.5 vol.% of magnetite. As SP particles have a higher susceptibility than SSD or MD particles (Worm, 1998), the content is probably overestimated. The mean of M_s ($0.32 \text{ Am}^2/\text{kg}$) obtained from the hysteresis data yields a consistent magnetite content of ~ 0.35 vol.%. For hematite, which contributes only very little to the χ values, we can estimate a content of ~ 5 vol.% from the XRD result of original red soil from the western basin. The HIRM allows another crude estimation of the hematite content. The result is consistent with the ~ 5 vol.% from XRD, if the M_{rs}/M_s ratio is ~ 0.05 (M_s for hematite: $0.4 \text{ Am}^2/\text{kg}$). This low M_{rs}/M_s ratio indicates very soft hematite, either existing as fine viscous grains or large MD grains. An alternative explanation would be an imperfect hematite with much lower M_s .

According to the position of the Caohai Lake, the predominant source area of the lake sediments is the nearby limestone terrain at the western basin (Figure 1). Magnetic concentration values in the Caohai Lake sediments vary by a factor of 3, and they are more than 1 order lower than the mean of the red soil. The quite high $\chi_{fd}\%$ values (mean 10.6%) indicate that a substantial part of the SP magnetite in the red soil material that was delivered to the lake is still existing after deposition.

The lake sediments show a similar appearance of magnetite nanoparticles in aggregates as revealed by the TEM observations (Figure 5a). However, other contributions strongly dilute the red soil material in the sediment. These contributions stem from the bedrock directly (measured carbonate content $\sim 25\%$), from enrichment of clay minerals and fragments of shell or snail shells. The amount of these nonferro(i)magnetic contributions is large, and therefore, the lower χ values in the lake sediments do not allow any statement on possible loss of magnetite during material transfer to the lake. However, the lower $\chi_{fd}\%$ of the Caohai Lake sediments compared to the red soil (mean of 10.6% vs. 17.8% at the western basin), the strong decrease of $\chi_{fd}\%$ values after CBD treatment (from 12.9% to 5.2%) compared to stable values for red soil of the western basin, a smaller decrease of χ values after CBD treatment (55% compared to 70%), and a much higher SIRM/ χ ratio (Figure 8f) are compatible with a higher relative contribution of larger-sized bedrock-derived MD magnetite to the magnetic properties in the lake sediments compared to red soil. From these data, one may conclude that a large part of the SP magnetite did not reach the lake. However, in the following section, we will present a model that could explain the observed difference of magnetic properties in the red soil and lake sediments without a loss of SP particles.

4.2. Magnetic Changes in Red Soil Material During Source-Sink Transfer

The appearance of the magnetite nanoparticles in the red soil and the Caohai Lake sediments is similar as observed by Lu et al. (2012) in the aforementioned thick red soil sequence in southwest China and by several authors in paleosols of the Chinese Loess Plateau (Ahmed & Maher, 2018; Chen et al., 2005; Liu et al., 2007). It was suggested that the nanoparticles are formed as extracellular precipitates due to bacterial activity, consisting of magnetite that is aging by maghemitization and final oxidation to hematite (Ahmed & Maher, 2018; Chen et al., 2005; Nie et al., 2010). Clear evidence for such bacterial-driven processes is provided by laboratory experiments, showing extracellular production of 20- to 50-nm large magnetite nanoparticles within days or weeks by Fe-reducing bacteria, arranged in framboidal aggregates with sizes <100 nm or even up to ~ 500 nm (O'Loughlin et al., 2015). The question of how the magnetite nanoparticles in the red soil of Heqing Basin were formed is not a key part of this paper, but in consideration of previous literature, we assume that they are a product of bacterial processes at the weathered limestone top, where iron is released from paramagnetic minerals through weathering of the limestone.

Comparison of the red soil and the Caohai Lake sediments allows the analysis of changes in the magnetic signatures during source-sink transfer. In this respect, the Caohai Lake acts as a sink of red soil material after translocation through wind and surface water. Any model explaining the magnetic changes of red soil material during this transfer must account for the decreased contribution of the SP fraction to the χ signal and the decreased $\chi_{fd}\%$ in the lake sediments. As mentioned above, the lower χ values of the lake sediments cannot be interpreted directly in terms of SP loss because of unknown dilution effects by other input materials.

Reflected light microscopy revealed that the larger magnetite particles in the Caohai Lake sediments are clearly detrital (i.e., not authigenic). Sediment input from far-distant sources such as eolian dust can be excluded (Yang et al., 2009), and besides the red soil, only very low-magnetic sedimentary rocks exist in

the catchment of Heqing Basin. Input of MD magnetite directly from bedrock weathering certainly contributes to the magnetic signal, but the question is whether this can significantly modulate the magnetic properties. In the red soil, the contribution of bedrock-inherited magnetite to the total magnetite fraction is minor as shown by the high $\chi_{\text{rd}}\%$ that is stable after CBD treatment. In contrast, the lower $\chi_{\text{rd}}\%$ of the lake sediments indicates roughly equal proportions of SP magnetite (pedogenic) and larger MD magnetite (bedrock related). To explain this by dilution due to direct input of MD magnetite released from limestones, the weathered bedrock has to deliver about the same amount of magnetite to the lake as the deposited red soil. In situ χ measurements of the limestone bedrock mostly yielded negative χ values. Taking a χ value of zero (which is higher than mostly measured in situ) and $\chi = -1.2 \times 10^{-5}$ SI for calcite (Schmidt et al., 2006) and assuming that the limestone is composed of nearly 100% calcite plus a minor magnetite fraction (i.e., ignoring a paramagnetic contribution), we yield a magnetite content of $<0.5 \times 10^{-3}$ vol.%, that is, 3 orders of magnitude less than the total magnetite content in red soil. Therefore, an at least 10^3 times larger volume of weathered and eroded limestones than red soil has to be delivered to the lake to achieve the necessary dilution. Such a dilution scenario can be ruled out, as red soil is widely covering the catchment area of Heqing Basin and is easily movable.

Differences of the magnetic characteristics between the red soil and the Caohai Lake sediments are therefore undoubtedly associated with changes of the nano-sized magnetite fraction. A possible process is dissolution of a large part of the fine magnetite particles in surface water or during the initial contact with lake water, as it was speculated by Hu et al. (2005). In order to test this, we filled several kg of red soil material from Heqing Basin into plastic containers and placed them permanently in the Caohai Lake at the sediment surface. The containers were perforated, allowing drainage by lake water. Measurements of samples taken every 6 months did not show significant changes after 4 years of permanent exposure. Although the experimental conditions do not reflect the conditions of fine particles suspended in the lake water or at the top of the sediment column, the absence of any change in magnetic concentration can at least be taken as a hint that dissolution is not a major mechanism during initial contact with lake water.

The XRF and LOI results and comparison with variations of magnetic parameters versus depth (Figure 8) allow further assessment of possible dissolution effects. Because in a reducing environment, the solubility of Fe and Mn increases but Mn is more readily affected, the Fe/Mn is used as an indicator for bottom-water oxygenation in lakes (e.g., Croudace & Rothwell, 2015; Koutsodendris et al., 2017; Morellón et al., 2016). On this basis, the Fe/Mn ratio suggests a gradual decrease of bottom-water oxygen content through time that can be either attributed to enhanced stratification in the water column or to deoxygenation from organic decay following enhanced biological productivity. Because the water depth of Caohai Lake is only 1–2 m, the first scenario can be firmly excluded; hence, an increase in biological productivity appears to be the driving mechanism behind the increase in reducing conditions in the lake. The biological activity appears particularly enhanced in the uppermost 10 cm if considering the increasing Si/Ti ratio, which has been widely used to differentiate between biogenic silica (predominantly related to diatom blooms in lakes) and detrital input reflected in Ti (e.g., Croudace & Rothwell, 2015; Koutsodendris et al., 2017; Morellón et al., 2016). Increased productivity in the uppermost 10 cm could be responsible for an intensification of oxygen reduction in the water column leading to an increase in organic material deposition and preservation. This view is supported by the elevated counts of S and Br, which can be attributed to increased pyrite formation in organic sediments and formation of strong covalent bonds with organic molecules, respectively (e.g., Croudace & Rothwell, 2015). The downward variation of the LOI that represents the organic carbon is well matching with the S and Br results.

Under such a reducing environment with increased influx of organic matter, dissolution of magnetite could be expected; this view is supported by the increase in the Fe/Ti ratio in the uppermost 10 cm, on the basis that Fe is redox sensitive in contrast to Ti (e.g., Aufgebauer et al., 2012; Croudace & Rothwell, 2015). Altogether, the XRF-based geochemical data suggest a strengthening of the oxygen depletion only in the uppermost 10 cm of the Caohai Lake sediment profile that could be responsible for magnetite dissolution. Comparing the geochemical and magnetic results, we notice that the geochemically indicated possible dissolution zone is at a much shallower level than the change in the χ values that represents a magnetite-concentration measure and is starting to increase substantially at ~20–25 cm. Moreover, the χ values are stable in the upper part until the top, whereas the LOI, Fe/Mn, S, Br, and in a less degree also Fe/Ti decrease at the top few cm.

The comparison of downcore variations strongly supports the view that the content of magnetite nanoparticles is not driven by dissolution effects, at least not to a degree that matters for the major changes of magnetic parameters. The broadband-frequency $\chi(f)$ results (Figure 7) confirm this conclusion. The lake sediments show a decrease of the $\chi(f)$ variation in the lower-frequency range, which indicates a depletion of the larger-sized SP contribution (Kodama, 2013), contrary of what is expected for dissolution that erases smaller grains faster.

The observed differences may be associated with oxidation of fine magnetite to hematite. The redox potential in red soil (Wheeler et al., 1999) favors low-temperature oxidation and transformation to hematite in situ. In fact, presence of hematite in the nanoparticles is indicated by the ELNES results (Figures 4d and 5c). According to modeling results of Ahmed and Maher (2018), complete oxidation of small (10 nm) magnetite particles into maghemite takes about 1 Myr at pH = 8, but it may also work much faster by bacterial activity (Byrne et al., 2015). As shown by the results from the vertical sections (Figure S7), there is no indication that cease of nano-magnetite production in red soil happens in situ. However, it can be speculated that bacterially induced production of nano-magnetite in red soil ceases when the red soil material is eroded and transferred to the sink (lake) by wind and surface water, while magnetite alteration still continues.

The higher SIRM/ χ and HIRM/ χ ratios (Figures 8f and 8g) in the Caohai Lake sediments compared to the red soil are compatible with such a scenario. However, it is questionable whether the time for oxidation during transfer from the origin to the sink is long enough to accomplish the conversion of a large part of magnetite into hematite. Moreover, it is unclear whether the hematite content in the red soil is generally related to oxidation of magnetite. If hematite originates from magnetite oxidation, be it via maghemite or by direct transformation, more nano-magnetite will lead to more hematite for the same degree of oxidation, and thus, the HIRM in the red soil should correlate positively with χ , the S ratio should be constant for different χ values, and in the lake sediments, the HIRM should inversely vary with χ , as higher χ values in the sediments implies that less nano-magnetite is oxidized to hematite. However, none of these relationships is observed (Figures 9b–9d). In summary, partial loss of magnetite by oxidation to hematite in red soil material during transfer to the lake is possible and is supported by the higher hematite content in the nanoparticles of aggregates as we observed by the ELNES results (Figures 4e and 5d), but it unlikely is the major process that causes the observed differences of magnetic properties in red soil and the Caohai Lake sediments.

The TEM results (Figures 4–6) and the broadband-frequency dependence $\chi(f)$ (Figure 7) provide the crucial clue to understand the key mechanism of magnetic differences. Close contact of nanoparticles within aggregates causes magnetostatic interaction between them, leading to larger effective grain sizes in terms of the domain state behavior than the physical size of the individual particles, as it is shown by theoretical models and experimental data studying such kind of ultrafine particle assemblages (Chen et al., 2008; Mørup et al., 2010; Souza et al., 2019). According to these results, variable arrangement of nanoparticles within different aggregates in the red soil and the Caohai Lake sediments will lead to a wide distribution of the effective grain sizes throughout the SP range, which can tail into the range of SSD behavior as shown by the cited works above. The resulting distribution of effective grain sizes will depend on the overall size of the aggregates, a denser or looser packing of the nanoparticles, and partial alteration (maghemitization or hematite formation) of the nano-magnetite. In our observations, the size of individual nanoparticles is similar in the red soil and the lake sediments, but their arrangement in the aggregates appears to be tighter in the red soil. Moreover, the sizes of the aggregates in the red soil are apparently larger. If these differences between the aggregates as seen in the TEM samples are representative of the materials as a whole, then it is plausible that mechanical stresses (e.g., during wind stress) led to differences in the aggregates. The donut-like small nanoparticle that are splattered around aggregates in the original red soil (Figure 6d) are not compatible with minimum-energy shapes that formed separately. They likely broke away from the aggregates, indicating that the aggregates are mechanically fragile.

The measured χ values are a function of the effective grain size and the applied frequency. The theoretical background has been presented by Worm (1998) and Shcherbakov and Fabian (2005). In Figure 10, we present a conceptual sketch that explains the expected dependence of χ values as a function of grain size and frequency. The dependence of χ versus grain size shows a peak-shaped behavior with the highest values and strong frequency dependence in the range of thermal activation, a constant and frequency-independent lower χ when approaching the SSD range, and decreasing χ values toward smaller SP particle sizes

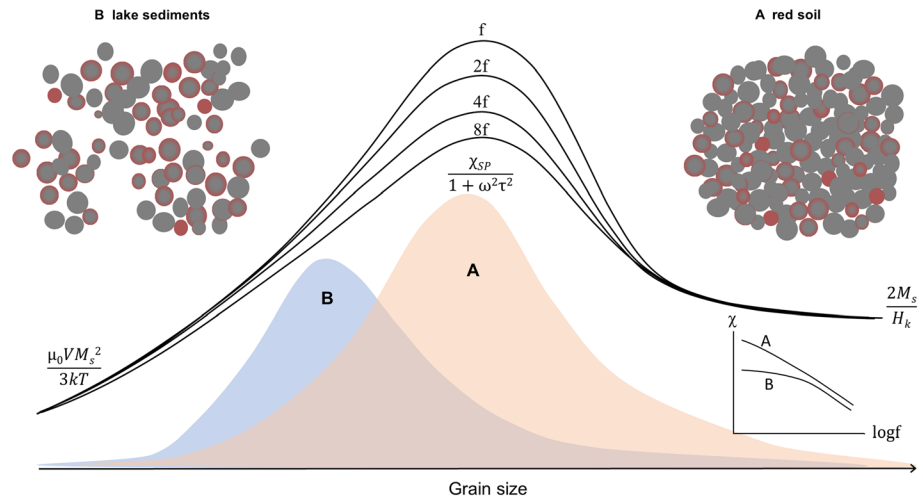


Figure 10. Conceptual sketch of the principle relationship of χ versus grain diameter (d) for four frequencies in logarithmically equal increments (increasing from f to $8f$), modified from Kodama (2013) and following the theory presented by Worm (1998) and Shcherbakov and Fabian (2005). The principle relationships for smaller SP grains (below thermal activation), SP grains in the range of thermal activation (frequency dependent; in-phase part), and larger grains in the SSD range are shown (M_s = saturation magnetization; H_k = microcoercivity; χ_{SP} = superparamagnetic susceptibility for zero frequency; V = grain volume; τ = relaxation time; T = temperature; f = frequency; ω = angular frequency; μ_0 = magnetic permeability of free space; k = Boltzmann constant). The orange and gray fields display schematic distributions of effective grain sizes of the nano-magnetite aggregates in red soil (A) and lake sediments (B), respectively. Aggregates in red soil are assumed to be tighter packed and possibly also larger than in lake sediments, and according to the ELNES results, more hematite is existing in the nanoparticles of the lake sediments.

(underlying χ relationships are given in Figure 10). For aggregates in State (A), with a denser packing of nanoparticles and less hematite, we assume a similar difference of χ values between the shown frequencies, whereas for aggregates in State (B), with looser packing and more hematite, the frequency dependence is stronger in the higher-frequency range. This will lead to a typical difference in the broadband-frequency dependence $\chi(f)$, together with a decrease of χ values due to the shift to smaller effective grain size, as shown by the principle $\chi(f)$ sketch (Figure 10).

Such difference can be seen in the measured broadband-frequency behavior of red soil and Caohai Lake sediment samples (Figure 7). The curves for red soil show an approximately linear decay of χ with $\log(f)$ throughout the frequency range of 125 to 16 kHz, whereas for the low χ samples from the lake sediments, the frequency dependence mainly occurs at $f > 1$ kHz. For the difference between red soil H and lake sediment L samples, the slope change is statistically significant at 95% confidence (Table S6). Kodama (2013) presented a method to determine the particle size from broadband-frequency data. Even without a quantitative inversion, it becomes obvious from $\chi(f)$ that the effective SP grain size is smaller in the Caohai Lake sediments than in the red soil, which can be explained by the less compact aggregates of nanoparticles in the lake sediments as observed in the TEM studies.

With this model, the macroscopic magnetic differences (χ , $\chi_{fd}\%$) between red soil and the Caohai Lake sediments can be explained without a loss of individual magnetite nanoparticles. The nano-magnetite fraction does not vanish, it simply becomes magnetically hidden as fining of the effective grain sizes due to increased separation of magnetite nanoparticles will lower the χ values (Figure 10) and will lead to a decline of $\chi_{fd}\%$. Partial transformation of magnetite to hematite as indicated by the ELNES results will cause an additional decrease of the χ value and $\chi_{fd}\%$. Hematite in the nanoparticles, either existing as full nanoparticles or as shells of magnetite cores (Figure 10), will also contribute to a shift toward smaller effective grain sizes through an increased distance between neighboring magnetite. Both the hematite fraction in the aggregates and the tighter or looser packing of nanoparticles affect the interaction between the magnetites and, therefore, will have an impact on the resulting $\chi_{fd}\%$ and χ values. How much both effects contribute to the observed differences between the red soil and Caohai Lake sediment properties is an open issue.

4.3. Relevance for Paleoclimate Studies

Heqing Basin accommodates two types of paleoclimate archives, the red soil and lake sediments, the latter concerning the modern lake sediments of Caohai Lake and the thick lacustrine sediment sequence accumulated in the large paleolake which existed in the basin throughout the Pleistocene until ~30 ka. The latter depends on the former by source-sink relationships. Lake sediments with red soil in the catchment is a frequently occurring setting in tropical and subtropical regions. Possible changes of pedogenic fine magnetite in red soil material, during transfer from the source (in situ) to the sink, and further changes in the lake have to be understood when employing magnetic proxies for paleoclimate studies. In Heqing Basin, red soil is the only relevant source of ferro(i)magnetic materials, and thus, our investigation area provides a unique opportunity to study possible magnetic changes in the red soil material, which happened during material transfer to lake. In the context of our study, the Caohai Lake acts as a sink of red soil material. It is not our aim to reconstruct the paleoenvironmental evolution as a function of the geological age, thus dating of the Caohai Lake sediments is not required for this purpose.

One of the questions regarding red soil archives is the possible environmental control of the amount of pedogenic ferro(i)magnetic minerals. In the Chinese Loess Plateau, paleorainfall was quantified from χ enhancement in the paleosols (Maher & Thompson, 1995). In red soil, the relationship between environmental conditions and fine magnetite production seems to be more complex. Liu et al. (2012) and Wang et al. (2013) suggested that magnetic signatures related to transformation of magnetite (maghemite) to hematite can be used to detect the degree of pedogenesis in vermiculated red soil. According to Wang et al. (2013), stronger pedogenesis leads to more hematite formed under warm climate with dry-moist seasonality. Yin et al. (2018) used the ratio of hematite and goethite contents in red soil as an indicator for climate conditions, determined by reflectance spectrophotometry, but they also concluded that its climate sensitivity is limited. As addressed above, the origin of magnetite or maghemite in soil has often been related to bacterial activity (Chen et al., 2005; Hu et al., 2015; Maher & Thompson, 1995), either by formation of extracellular SP magnetite as a metabolism product (Ahmed & Maher, 2018; Lovley et al., 1987; Sundaram et al., 2012) or intracellular magnetosomes in the SSD range (Fassbinder et al., 1990). In the studied red soil of Heqing Basin, the observed aggregates of nanoparticles likely represent extracellular magnetite; magnetosomes were not detected. The appearance of the aggregates resembles Fe-oxyhydroxide nanoparticle aggregates of up to >100 nm large attached to the outer membrane of living bacteria (Luef et al., 2013), which could be a hint on the origin of the aggregates in the red soil. This issue is an exciting research question for future study, but it is beyond the scope of this paper.

The about threefold higher mean χ values of red soil above the limestone bedrock at the western basin ($\chi = 1,085 \times 10^{-8} \text{ m}^3/\text{kg}$) compared to red soil on sandstone and conglomerate at the eastern basin ($\chi = 302 \times 10^{-8} \text{ m}^3/\text{kg}$) indicate that there is no matching climate-related χ enhancement. As calcite dissolves relatively fast during weathering, more efficient release of Fe is expected for limestone bedrock. However, the spatial distribution of the χ values (Figure 1 and Tables 1 and S1) clearly shows that the amount of pedogenic magnetite does not only strongly differ for the different bedrock types but also varies within the same type (standard deviation of χ for red soil on both limestones and sandstones/conglomerates is 53% of the mean χ value). Therefore, neither χ values nor $\chi_{\text{fd}}\%$ of red soil are suitable to discriminate different environmental conditions. If hematite derives from alteration of fine magnetite, as suggested by earlier studies of red soil (Liu et al., 2012; Wang et al., 2013) and also proposed by Torrent et al. (2006) for aerobic soil, the relative proportions of fine magnetite and hematite could provide useful information on environmental conditions, and the HIRM/ χ ratio may be a suitable proxy. However, the bivariate plot of HIRM versus χ (Figure 9b) shows strong scattering of the data.

In contrast, there is a good linear relationship of SIRM and χ (Figure 9d) for the red soil above limestones ($r = 0.92$) and still reasonable for red soil above sandstones/conglomerates ($r = 0.64$). The latter correlation is probably lower because of the more variable bedrock lithology. The SIRM/ χ ratio is strongly different for the limestones (4.20 kA/m) and sandstones/conglomerates (6.52 kA/m), but if it is possible to establish separate transfer functions for different bedrock types, this ratio may be a suitable proxy parameter for the degree of pedogenesis as previously suggested (Liu et al., 2012; Wang et al., 2013). The scattered HIRM versus χ distribution points out that there is no simple systematic mechanism of magnetite-to-hematite transformation. The about 1:10 molar ratio of magnetite (estimated from χ and M_s) and hematite

(estimated from XRD) contents in the red soil suggests that only a smaller part of the hematite sits in the nanoparticle aggregates.

But why does the SIRM correlate with χ ? If there is a climate-specific development of the nanoparticle aggregates, expressed by denser/looser packing of nanoparticles, different size of aggregates, or different proportion of hematite, a characteristic SP-SSD behavior distribution (according to the schematic relationship shown in Figure 10) could be imprinted in the relative proportions of SSD magnetite (controlling SIRM) and SP magnetite (dominating χ) behaviors. In such case, the SIRM/ χ ratio is mainly dependent on the nano-magnetite in the aggregates, with only very little contribution of hematite. Further studies are needed to understand the underlying processes and to develop meaningful transfer functions.

Studies of lake sediments in settings with red soil as the dominating source material, as in Heqing Basin, suffer from several uncertainties. According to our model presented in section 4.2, the pedogenic fine magnetite fraction of the red soil material is to a large extent still existing after deposition. However, due to the decreased effective magnetic grain size of the nano-magnetite aggregates, it is less contributing to the χ values and $\chi_{fd}\%$ (Figure 10). Comparison of geochemical and magnetic parameter variations throughout the Caohai Lake sediment sequence (Figures 8a–8c) indicates that there is no substantial loss of the nano-magnetite by dissolution. Magnetic concentration values in the lower part of the Caohai Lake sediments are about double as high as in the upper part (Figures 8a–8c). This variation with depth may indicate a response to climate change or a change in the hydrological conditions during the deposition period, residing in both the nanoparticle aggregates and the bedrock-inherited MD magnetite. As it is a mixed signal, the underlying control of magnetic properties requires further detailed study, which is beyond the scope of this paper.

What is the meaning of the new results for the interpretation of magnetic proxies in the long Core-HQ from the large paleolake in Heqing Basin (Figure 1)? Hu et al. (2015) concluded from the very low $\chi_{fd}\%$ throughout the 168-m-long sequence (mean $\chi_{fd}\% \sim 2.5\%$) that SP magnetite derived from red soil is absent, and they reconstructed paleo-humidity conditions assuming an alteration mechanism of the remaining bedrock-inherited larger-sized magnetite. Results from other lakes in southwestern China, with similar setting as Heqing Basin, suggest that SP fractions are indeed effectively dissolved below a certain depth in the sediment column. In Erhai Lake, this depth occurs at ~ 50 – 60 cm (Dearing et al., 2008) and, in Xingyun Lake, below ~ 1 -m sediment depth (Chen et al., 2014), both lakes having a similar size as the Heqing paleolake. In the modern Caohai Lake, efficient dissolution is not observed, which could be due to the only ~ 0.5 -m sediment thickness. Moreover, redox conditions in the small Caohai Lake with low water depth cannot directly be compared to the much larger and deeper Heqing paleolake.

According to our model presented in section 4.2, there is a possible completely different explanation. Advanced disintegration of the aggregates of magnetite nanoparticles could drive the effective magnetic grain size to an SP range with low $\chi_{fd}\%$ (i.e., a smaller effective size). For this reason, the validity of the paleo-humidity reconstruction of Hu et al. (2015) for the ~ 900 - to 30-ka period in Core-HQ, based on the assumption that SP magnetite from red soil has been erased, is challenged by our new results. A substantial SP magnetite fraction originating from disintegrated aggregates may still exist in the sediments, forming separated nanoparticles or small aggregates. Although not contributing to magnetic remanence parameters, this SP fraction would carry part of the χ signal on which Hu et al. (2015) partly built their interpretation.

5. Conclusions

Heqing Basin is a useful example for studying changes of magnetic properties in a setting of lake sediments with red soil as the only important source of ferro(i)magnetic input. The results detect the nature and macroscopic expression of magnetic changes in red soil material during transfer from the origin to the sink (Caohai Lake sediments), with implications for paleoclimate studies:

1. Highly magnetic red soil on low-magnetic sedimentary bedrock with up to $\sim 0.5\%$ magnetite (according to χ and M_s) occurs throughout the Heqing Basin catchment. Extremely high $\chi_{fd}\%$ (~ 15 – 20%) shows that SP magnetite is strongly dominating, which is likely an extracellular product of bacterial activity during pedogenesis.
2. The TEM results reveal ~ 100 -nm large aggregates of mainly ~ 10 - to 15 -nm sized nanoparticles in the red soil and in the Caohai Lake sediments. The nanoparticles in the aggregates are tighter packed in red soil

than in the lake sediments, and the aggregates in the red soil appear to be larger. ELNES results identify the nanoparticles as magnetite and/or maghemite (which cannot be discriminated), with higher contribution of hematite in aggregates of the Caohai Lake sediments. Interaction of the nano-magnetite particles leads to a wide range of effective grain sizes in terms of their domain state behavior. The effective grain size is naturally larger than the physical size of individual nanoparticles and tails into the SSD range. Interaction is less for looser packing and for larger hematite content that creates larger distances between magnetites. This model explains the observed differences of macroscopic magnetic characteristics between red soil and lake sediments by a shift of the effective grain size distribution toward smaller size. The results of broadband-frequency dependence of χ support the model.

3. Spatial distributions of magnetic parameters in the red soil around Heqing Basin clearly show that the amount of pedogenically produced nano-magnetite is bedrock dependent and even varies within the same bedrock type. The SIRM/ χ ratio is relatively constant for red soil above the same bedrock type, it is assumed to be controlled by a shift of the specific SP-SSD distribution in the aggregates possibly related to environmental conditions and is therefore a potential paleoclimate proxy. Further research is required to elucidate whether bedrock-specific transfer functions can be determined.
4. The magnetic signature of the Caohai Lake sediments is controlled by both magnetite nanoparticle aggregates and MD magnetite inherited from bedrock weathering. A composed paleoclimate signature of the magnetic parameter variations might exist, but a complex control mechanism is expected, which requires further research. The validity of the paleoclimate reconstruction of Hu et al. (2015) from the 168-m-long Core-HQ in Heqing Basin, spanning the period of ~900–30 ka, is challenged. The underlying assumption of SP magnetite extinction by dissolution, derived from low χ_{fd} % values, could be wrong. According to the new results, disintegrated magnetite aggregates may represent an SP state with low χ_{fd} %, without loss of nanoparticles.

Data Availability Statement

The data used in this paper are displayed in Figures 1–10 and Table 1, and primary data are listed in Tables S1–S7, also shown in Figures S1–S7. The data are available in the Mendeley database for public download (<https://doi.org/10.17632/m4gvh8p4cf>).

Acknowledgments

This research was supported by the National Natural Science Foundation of China (41572152), the German Research Foundation (DFG; AP 34/44-1), and the Chinese Academy of Sciences Visiting Professorship for Senior International Scientists (2012T1Z0004 and 131432WGZJTPYJY20150002). We thank James Byrne and Julian Sorwat for their help in CBD treatment, Timm Bayer for preparation of samples for TEM analysis, and Daniel Buchner for enabling the carbonate and OC analysis. Open access funding enabled and organized by Projekt DEAL.

References

- Ahmed, I. A. M., & Maher, B. A. (2018). Identification and paleoclimatic significance of magnetite nanoparticles in soils. *Proceedings of the National Academy of Sciences*, *115*(8), 1736–1741. <https://doi.org/10.1073/pnas.1719186115>
- An, Z. S., Clemens, S. C., Shen, J., Qiang, X., Jin, Z. D., Sun, Y. B., et al. (2011). Glacial-interglacial Indian summer monsoon dynamics. *Science*, *333*(6043), 719–723. <https://doi.org/10.1126/science.1203752>
- Aragón, R., Buttrey, D. J., Shephard, J. P., & Honig, J. M. (1985). Influence of non-stoichiometry on the Verwey transition. *Physical Review B*, *31*(1), 430–436. <https://doi.org/10.1103/PhysRevB.31.430>
- Aufgebauer, A., Panagiotopoulos, K., Wagner, B., Schaebitz, F., Viehberg, F. A., & Vogel, H. (2012). Climate and environmental change in the Balkans over the last 17 ka recorded in sediments from Lake Prespa (Albania/F.Y.R. of Macedonia/Greece). *Quaternary International*, *274*, 122–135. <https://doi.org/10.1016/j.quaint.2012.02.015>
- Bengtsson, L. (1986). *Chemical analysis: Handbook of Holocene palaeoecology and palaeohydrology*, 423–451. Chichester, UK: John Wiley and Sons.
- Bilardello, D., & IRM (2020). Practical magnetism II: Humps and a bump, the maghemite song. *The IRM Quarterly*, *30*(1), 15–17. ISSN: 2152-1972
- Bloemendal, J., King, J. W., Hall, F. R., & Doh, S. J. (1992). Rock magnetism of Late Neogene and Pleistocene deep-sea sediments: Relationship to sediment source, diagenetic processes, and sediment lithology. *Journal of Geophysical Research*, *97*(B4), 4361–4375. <https://doi.org/10.1029/91JB03068>
- Bowles, J., Jackson, M., Chen, A., & Solheid, P. (2009). Interpretation of low-temperature data part 1: Superparamagnetism and paramagnetism. *The IRM quarterly*, *19*(3), 1–11. ISSN: 2152-1972
- Bowles, J. F. W., Howie, R. A., Vaughan, D. J., & Zussman, J. (2011). *Rock-forming minerals: Non-silicates: Oxides, hydroxides and sulphides*. London, UK: Geological Society of London.
- Bronger, A., & Bruhn-Lobin, N. (1997). Paleopedology of Terrae rossae—Rhodoxerals from Quaternary calcarenites in NW Morocco. *Catena*, *28*(3–4), 279–295. [https://doi.org/10.1016/S0341-8162\(96\)00043-4](https://doi.org/10.1016/S0341-8162(96)00043-4)
- Byrne, J., Klueglein, N., Pearce, C., Rosso, K. M., Appel, E., & Kappler, A. (2015). Redox cycling of Fe (II) and Fe (III) in magnetite by Fe-metabolizing bacteria. *Science*, *347*(6229), 1473–1476. <https://doi.org/10.1126/science.aaa4834>
- Chen, D. X., Sanchez, A., Xu, H., Gu, H. C., & Shi, D. L. (2008). Size-independent residual magnetic moments of colloidal Fe₃O₄-polystyrene nanospheres detected by ac susceptibility measurements. *Journal of Applied Physics*, *104*(9), 093902. <https://doi.org/10.1063/1.3005988>
- Chen, F. H., Chen, X. M., Chen, J. H., Zhou, A. E., Wu, D., Tang, L. Y., et al. (2014). Holocene vegetation history, precipitation changes and Indian summer monsoon evolution documented from sediments of Xingyun Lake, south-west China. *Journal of Quaternary Science*, *29*(7), 661–674. <https://doi.org/10.1002/jqs.2735>

- Chen, T. H., Xu, H. F., Xie, Q. Q., Chen, J., Ji, J. F., & Lu, H. Y. (2005). Characteristics and genesis of maghemite in Chinese loess and paleosols: Mechanism for magnetic susceptibility enhancement in paleosols. *Earth and Planetary Science Letters*, *240*(3–4), 790–802. <https://doi.org/10.1016/j.epsl.2005.09.026>
- Colliex, C., Manoubi, T., & Ortiz, C. (1991). Electron-loss-spectroscopy near-edge fine structures in the iron-oxygen system. *Physical Review B*, *44*(20), 11,402–11,411. <https://doi.org/10.1103/PhysRevB.44.11402>
- Croudace, I. W., & Rothwell, R. G. (Eds.) (2015). Micro-XRF studies of sediment cores. In *Developments in paleoenvironmental research* (Vol. 17, pp. 507–534). Dordrecht: Springer. <https://doi.org/10.1007/978-94-017-9849-5>
- Day, R., Fuller, M., & Schmidt, V. A. (1977). Hysteresis properties of titanomagnetites: Grain size and composition dependence. *Physics of the Earth and Planetary Interiors*, *13*(4), 260–267. [https://doi.org/10.1016/0031-9201\(77\)90108-X](https://doi.org/10.1016/0031-9201(77)90108-X)
- Dean, W. E. (1974). Determination of carbonate and organic-matter in calcareous sediments and sedimentary-rocks by loss on ignition—Comparison with other methods. *Journal of Sedimentary Petrology*, *44*(1), 242–248. <https://doi.org/10.1306/74D729D2-2B21-11D7-8648000102C1865D>
- Dearing, J. A., Dann, R. J. L., Hay, K., Lees, J., Loveland, P. J., Maher, B. A., & O'Grady, K. (1996). Frequency-dependent susceptibility measurements of environmental materials. *Geophysical Journal International*, *124*(1), 228–240. <https://doi.org/10.1111/j.1365-246X.1996.tb06366.x>
- Dearing, J. A., Jones, R. T., Shen, J., Yang, X., Boyle, J. F., & Foster, G. C. (2008). Using multiple archives to understand past and present climate-human-environment interactions: The Lake Erhai catchment, Yunnan Province, China. *Journal of Paleolimnology*, *40*(1), 3–31. <https://doi.org/10.1007/s10933-007-9182-2>
- Deng, C. L., Hao, Q. Z., Guo, Z. T., & Zhu, R. X. (2019). Quaternary integrative stratigraphy and timescale of China. *Science China Earth Sciences*, *62*(1), 324–348. <http://doi.org/10.1007/s11430-017-9195-4>
- Deng, C. L., Zhu, R. X., Verosub, K. L., Singer, M. J., & Vidic, N. J. (2004). Mineral magnetic properties of loess/paleosol couplets of the central loess plateau of China over the last 1.2 Myr. *Journal of Geophysical Research*, *109*, B01103. <https://doi.org/10.1029/2003JB002532>
- Dunlop, D. J. (2002). Theory and application of the Day plot (M_{rs}/M_s versus H_{cr}/H_c) I. Theoretical curves and tests using titanomagnetite data. *Journal of Geophysical Research*, *107*, B3. <https://doi.org/10.1029/2001JB000486>
- Fassbinder, J. W. E., Stanjek, H., & Vali, H. (1990). Occurrence of magnetic bacteria in soil. *Nature*, *343*(6254), 161–163. <https://doi.org/10.1038/343161a0>
- Feenstra, A., Sämann, S., & Wunder, B. (2005). An experimental study of Fe–Al solubility in the system corundum–hematite up to 40 kbar and 1300°C. *Journal of Petroleum Science and Engineering*, *46*(9), 1881–1892. <https://doi.org/10.1093/petrology/egi038>
- Feng, J. L., Cui, Z. J., & Zhu, L. P. (2009). Origin of terra rossa over dolomite on the Yunnan–Guizhou Plateau, China. *Geochemical Journal*, *43*(3), 151–166. <https://doi.org/10.2343/geochemj.1.0014>
- Gasse, F., Arnold, M., Fontes, J. C., Fort, M., Gibert, E., Huc, A., et al. (1991). A 13,000-year climate record from western Tibet. *Nature*, *353*(6346), 742–745. <https://doi.org/10.1038/353742a0>
- Geiss, C. E., Umbanhowar, C. E., Camill, P., & Banerjee, S. K. (2003). Sediment magnetic properties reveal Holocene climate change along the Minnesota prairie-forest ecotone. *Journal of Paleolimnology*, *30*(2), 151–166. <https://doi.org/10.1023/A:1025574100319>
- Golla-Schindler, U., Hinrichs, R., Bomati-Miguel, O., & Putnis, A. (2006). Determination of the oxidation state for iron oxide minerals by energy-filtering TEM. *Micron*, *37*(5), 473–477. <https://doi.org/10.1016/j.micron.2005.11.002>
- Harrison, R. J., & Feinberg, J. M. (2008). FORCinel: An improved algorithm for calculating first-order reversal curve distributions using locally weighted regression smoothing. *Geochimistry, Geophysics, Geosystems*, *9*, Q05016. <https://doi.org/10.1029/2008GC001987>
- He, Z. L., Zhang, M. K., & Wilson, M. J. (2004). Distribution and classification of red soils in China. In M. J. Wilson, Z. He, X. Yang (Eds.), *The red soils of China* (pp. 29–33). Dordrecht: Springer. https://doi.org/10.1007/978-1-4020-2138-1_3
- Heiri, O., Lotter, A. F., & Lemcke, G. (2001). Loss on ignition as a method for estimating organic and carbonate content in sediments: Reproducibility and comparability of results. *Journal of Paleolimnology*, *25*(1), 101–110. <https://doi.org/10.1023/A:1008119611481>
- Hu, S. Y., Goddu, S. R., Appel, E., Verosub, K., Yang, X. D., & Wang, S. (2005). Palaeoclimatic changes over past one million years derived from lacustrine sediments of Heqing Basin (Yunnan, China). *Quaternary International*, *136*(1), 123–129. <https://doi.org/10.1016/j.quaint.2004.11.013>
- Hu, S. Y., Goddu, S. R., Herb, C., Appel, E., Gleixner, G., Wang, S. M., et al. (2015). Climate variability and its magnetic response recorded in a lacustrine sequence in Heqing basin at the SE Tibetan Plateau since 900 ka. *Geophysical Journal International*, *201*(1), 444–458. <https://doi.org/10.1093/gji/ggv033>
- Hunt, C. P., Singer, M. J., Kletetschka, G., Tenpas, J., & Verosub, K. L. (1995). Effect of citrate-bicarbonate-dithionite treatment on fine-grained magnetite and maghemite. *Earth and Planetary Science Letters*, *130*(1–4), 87–94. [https://doi.org/10.1016/0012-821X\(94\)00256-X](https://doi.org/10.1016/0012-821X(94)00256-X)
- Jiang, Z. X., Liu, Q. S., Barrón, V., Torrent, J., & Yu, Y. J. (2012). Magnetic discrimination between Al-substituted hematites synthesized by hydrothermal and thermal dehydration methods and its geological significance. *Journal of Geophysical Research*, *117*, B02102. <https://doi.org/10.1029/2011JB008605>
- Kern, O. A., Koutsodendris, A., Mächtle, B., Christanis, K., Schukraft, G., Scholz, C., et al. (2019). X-ray fluorescence core scanning yields reliable semiquantitative data on the elemental composition of peat and organic-rich lake sediments. *Science of the Total Environment*, *697*, 134110. <https://doi.org/10.1016/j.scitotenv.2019.134110>
- Khadkikar, A. S., & Basavaiah, N. (2004). Morphology, mineralogy and magnetic susceptibility of epikarst-Terra Rossa developed in late Quaternary aeolianite deposits of southeastern Saurashtra, India. *Geomorphology*, *58*(1–4), 339–355. <https://doi.org/10.1016/j.geomorph.2003.07.001>
- Kodama, K. (2013). Application of broadband alternating current magnetic susceptibility to the characterization of magnetic nanoparticles in natural materials. *Journal of Geophysical Research: Solid Earth*, *118*, 1–12. <https://doi.org/10.1029/2012JB009502>
- Koutsodendris, A., Brauer, A., Reed, J. M., Plessen, B., Friedrich, O., Hennrich, B., et al. (2017). Climate variability in SE Europe since 1450 AD based on a varved sediment record from Etoliko Lagoon (western Greece). *Quaternary Science Reviews*, *159*, 63–76. <https://doi.org/10.1016/j.quascirev.2017.01.010>
- Koutsodendris, A., Sachse, D., Appel, E., Herb, C., Fischer, T., Fang, X. M., & Pross, J. (2018). Prolonged monsoonal moisture availability preconditioned glaciation of the Tibetan Plateau during the Mid-Pleistocene transition. *Geophysical Research Letters*, *45*, 13,020–13,030. <https://doi.org/10.1029/2018GL07930300>
- Lavrieux, M., Birkholz, A., Meusburger, K., Wiesenberg, G. L. B., Gilli, A., Stamm, C., & Alewel, C. (2019). Plants or bacteria? 130 years of mixed imprints in Lake Baldegg sediments (Switzerland), as revealed by compound-specific isotope analysis (CSIA) and biomarker analysis. *Biogeosciences*, *16*(10), 2131–2146. <https://doi.org/10.5194/bg-16-2131-2019>
- Liu, C. C., Deng, C. L., & Liu, Q. S. (2012). Mineral magnetic studies of the vermiculated red soils in southeast China and their paleoclimatic significance. *Palaeogeography, Palaeoclimatology, Palaeoecology*, *329–330*, 173–183. <https://doi.org/10.1016/j.palaeo.2012.02.035>

- Liu, Q. S., Deng, C. L., Torrent, J., & Zhu, R. X. (2007). Review of recent developments in mineral magnetism of the Chinese loess. *Quaternary Science Reviews*, 26(3–4), 368–385. <https://doi.org/10.1016/j.quascirev.2006.08.004>
- Liu, Z. F., Ma, J. L., Wie, G. J., Liu, Q. S., Jiang, Z. X., Ding, X., et al. (2017). Magnetism of a red soil core derived from basalt, northern Hainan Island, China: Volcanic ash versus pedogenesis. *Journal of Geophysical Research: Solid Earth*, 122, 1677–1696. <https://doi.org/10.1002/2016JB013834>
- Lovley, D. R., Stolz, J. F., Nord, G. L. Jr., & Phillips, E. J. P. (1987). Anaerobic production of magnetite by a dissimilatory iron-reducing microorganism. *Nature*, 330(6145), 252–254. <https://doi.org/10.1038/330252a0>
- Lu, S. G., Chen, D. J., Wang, S. Y., & Liu, Y. D. (2012). Rock magnetism investigation of highly magnetic soil developed on calcareous rock in Yun-Gui Plateau, China: Evidence for pedogenic magnetic minerals. *Journal of Applied Geophysics*, 77, 39–50. <https://doi.org/10.1016/j.jappgeo.2011.11.008>
- Luef, B., Fakra, S. C., Csencsits, R., Wrighton, K. C., Williams, K. H., Wilkins, M. J., et al. (2013). Iron-reducing bacteria accumulate ferric oxyhydroxide nanoparticle aggregates that may support planktonic growth. *The ISME Journal*, 7(2), 338–350. <https://doi.org/10.1038/ismej.2012.103>
- Maher, B. A. (1998). Magnetic properties of modern soils and Quaternary loessic paleosols: Paleoclimatic implications. *Palaeogeography, Palaeoclimatology, Palaeoecology*, 137(1–2), 25–54. [https://doi.org/10.1016/S0031-0182\(97\)00103-X](https://doi.org/10.1016/S0031-0182(97)00103-X)
- Maher, B. A., & Taylor, R. M. (1988). Formation of ultrafine-grained magnetite in soils. *Nature*, 336(6197), 368–370. <https://doi.org/10.1038/336368a0>
- Maher, B. A., & Thompson, R. (1995). Paleorainfall reconstructions from pedogenic magnetic susceptibility variations in the Chinese loess and paleosols. *Quaternary Research*, 44(3), 383–391. <https://doi.org/10.1006/qres.1995.1083>
- Maxbauer, D. P., Feinberg, J. M., & Fox, D. L. (2016). MAX UnMix: A web application for unmixing magnetic coercivity distributions. *Computers & Geosciences*, 95, 140–145. <https://doi.org/10.1016/j.cageo.2016.07.009>
- Mehra, O. P., & Jackson, M. L. (1960). Iron oxide removal from soils and clays by a dithionite-citrate system buffered with sodium bicarbonate. *Clays and Clay Minerals*, 7, 317–327. <https://doi.org/10.1016/B978-0-08-009235-5.50026-7>
- Morellón, M., Anselmetti, F. S., Ariztegui, D., Brushulli, B., Sinopoli, G., Wagner, B., et al. (2016). Human-climate interactions in the central Mediterranean region during the last millennia: The laminated record of Lake Butrint (Albania). *Quaternary Science Reviews*, 136, 134–152. <https://doi.org/10.1016/j.quascirev.2015.10.043>
- Morup, S., Hansen, M. F., & Frandsen, C. (2010). Magnetic interactions between nanoparticles. *Beilstein Journal of Nanotechnology*, 1, 182–190. <https://doi.org/10.3762/bjnano.1.22>
- Nie, J. S., Song, Y. G., King, J. W., & Egli, R. (2010). Consistent grain size distribution of pedogenic maghemite of surface soils and Miocene loessic soils on the Chinese Loess Plateau. *Journal of Quaternary Science*, 25(3), 261–266. <https://doi.org/10.1002/jqs.1304>
- Oldfield, F., & Robinson, S. G. (1985). Geomagnetism and paleoclimate. In M. J. Tooley & G. M. Sheail (Eds.), *The Climatic scene* (pp. 186–205). Boston: Allen & Unwin.
- O'Loughlin, E. J., Gorski, C. A., & Scherer, M. M. (2015). Effects of phosphate on secondary mineral formation during the bioreduction of akaganeite (β -FeOOH): Green rust versus framboidal magnetite. *Current Inorganic Chemistry*, 5(3), 214–224. <https://doi.org/10.2174/1877944105666150421001126>
- O'Neill, H. S. C., & Dollase, W. A. (1994). Crystal structures and cation distributions in simple spinels from powder XRD structural refinements: MgCr_2O_4 , ZnCr_2O_4 , Fe_3O_4 and the temperature dependence of the cation distribution in ZnAl_2O_4 . *Physics and Chemistry of Minerals*, 20(8), 541–555. <https://doi.org/10.1007/BF00211850>
- Pecharmán, C., González-Carreño, T., & Iglesias, J. E. (1995). The infrared dielectric properties of maghemite, γ - Fe_2O_3 , from reflectance measurement on pressed powders. *Physics and Chemistry of Minerals*, 22(1), 21–29. <https://doi.org/10.1007/BF00202677>
- Peck, J. A., King, J. W., Colman, S. M., & Kravchinsky, V. A. (1994). A rock magnetic record from Lake Baikal, Siberia: Evidence for Late Quaternary climatic change. *Earth and Planetary Science Letters*, 122(1–2), 221–238. [https://doi.org/10.1016/0012-821X\(94\)90062-0](https://doi.org/10.1016/0012-821X(94)90062-0)
- Readman, P. W., & O'Reilly, W. (1972). Magnetic properties of oxidized (cation-deficient) titanomagnetites, $(\text{Fe,Ti}, \square)\text{O}_4$. *Journal of Geomagnetism and Geoelectricity*, 24(1), 69–90. <https://doi.org/10.5636/jgg.24.69>
- Roberts, A. P., Tauxe, L., Heslop, D., Zhao, X., & Jiang, Z. X. (2018). A critical appraisal of the “Day” diagram. *Journal of Geophysical Research: Solid Earth*, 124, 5286–5314. <https://doi.org/10.1029/2018JB017049>
- Schmidt, V., Günther, D., & Hirt, A. M. (2006). Magnetic anisotropy of calcite at room-temperature. *Tectonophysics*, 418(1–2), 63–73. <https://doi.org/10.1016/j.tecto.2005.12.019>
- Shcherbakov, V. P., & Fabian, K. (2005). On the determination of magnetic grain-size distributions of superparamagnetic particle ensembles using the frequency dependence of susceptibility at different temperatures. *Geophysical Journal International*, 162(3), 736–746. <https://doi.org/10.1111/j.1365-246X.2005.02603.x>
- Snowball, I. F. (1993). Mineral magnetic properties of Holocene lake and soils from the Karsa Valley, Lappland, Sweden, and their relevance to paleoenvironmental reconstruction. *Terra Nova*, 5(3), 258–270. <https://doi.org/10.1111/j.1365-3121.1993.tb00257.x>
- Song, Y., Hao, Q. Z., Ge, J. Y., Zhao, D., Zhang, Y., Li, Q., et al. (2014). Quantitative relationships between magnetic enhancement of modern soils and climatic variables over the Chinese Loess Plateau. *Quaternary International*, 334–335, 119–131. <https://doi.org/10.1016/j.quaint.2013.12.010>
- Souza, C. M., Pedrosa, S. S., Carriço, A. S., Rebouças, G. O. G., & Dantas, A. L. (2019). Thermal hysteresis of superparamagnetic Gd nanoparticle clusters. *Physical Review B*, 99(17), 174441. <https://doi.org/10.1103/PhysRevB.99.174441>
- Sundaram, P. A., Augustine, R., & Kannan, M. (2012). Extracellular biosynthesis of iron oxide nanoparticles by *Bacillus subtilis* strains isolated from rhizosphere soil. *Biotechnology and Bioengineering*, 17(4), 835–840. <https://doi.org/10.1002/s12257-011-0582-9>
- Tabor, N. J., & Myers, T. S. (2015). Paleosols as indicators of paleoenvironment and paleoclimate. *Annual Review of Earth and Planetary Sciences*, 43(1), 333–361. <https://doi.org/10.1146/annurev-earth-060614-105355>
- Torrent, J., Barron, V., & Liu, Q. S. (2006). Magnetic enhancement is linked to and precedes hematite formation in aerobic soil. *Geophysical Research Letters*, 33, L02402. <https://doi.org/10.1029/2005GL024818>
- van Oorschot, I. H. M., & Dekkers, M. L. (1999). Dissolution behaviour of fine-grained magnetite and maghemite in the citrate-bicarbonate-dithionite extraction method. *Earth and Planetary Science Letters*, 167, 283–295. [https://doi.org/10.1016/S0012-821X\(99\)00033-3](https://doi.org/10.1016/S0012-821X(99)00033-3)
- Wang, S. Y., Lin, S., & Lu, S. G. (2013). Rock magnetism, iron oxide mineralogy and geochemistry of Quaternary red earth in central China and their paleopedogenic implication. *Palaeogeography, Palaeoclimatology, Palaeoecology*, 379–380, 95–103. <https://doi.org/10.1016/j.palaeo.2013.04.010>
- Wheeler, D. B., Thompson, J. A., & Bell, J. C. (1999). Laboratory comparison of soil redox conditions between red soils and brown soils in Minnesota, USA. *Wetlands*, 19(3), 607–616. <https://doi.org/10.1007/BF03161698>

- Worm, H. U. (1998). On the superparamagnetic-stable single domain transition for magnetite, and frequency dependence of susceptibility. *Geophysical Journal International*, *133*(1), 201–206. <https://doi.org/10.1046/j.1365-246X.1998.1331468.x>
- Xiao, X. Y., Shen, J., Wang, S. M., Xiao, H. F., & Tong, G. B. (2010). The variation of the southwest monsoon from high resolution pollen record in Heqing Basin, Yunnan Province, China for the last 2.78 Ma. *Palaeogeography, Palaeoclimatology, Palaeoecology*, *287*(1–4), 45–57. <https://doi.org/10.1016/j.palaeo.2010.01.013>
- Yaalon, D. H. (1997). Soils in the Mediterranean region: What makes them different? *Catena*, *28*(3–4), 157–169. [https://doi.org/10.1016/S0341-8162\(96\)00035-5](https://doi.org/10.1016/S0341-8162(96)00035-5)
- Yang, T., Liu, Q. S., Zeng, Q. L., & Chan, L. S. (2009). Environmental magnetic responses of urbanization processes: Evidence from lake sediments in East Lake, Wuhan, China. *Geophysical Journal International*, *179*(2), 873–886. <https://doi.org/10.1111/j.1365-246X.2009.04315.x>
- Yin, K., Hong, H. L., Algeo, T. J., Churchman, G. J., Li, Z. H., Zhu, Z. M., et al. (2018). Fe-oxide mineralogy of the Jiujiang red earth sediments and implications for Quaternary climate change, southern China. *Scientific Reports*, *8*(1), 3610. <http://doi.org/10.1038/s41598-018-20119-4>